Implementing the homography-based global HR-EBSD/TKD approach

Clément Ernould[a,b], Benoît Beausir[a,b,*], Jean-Jacques Fundenberger[a,b], Vincent Taupin[a,b], and Emmanuel Bouzy[a,b]

[a]Université de Lorraine, CNRS, LEM3, Metz, France
[b]Laboratory of Excellence on Design of Alloy Metals for low-mAss Structures (DAMAS), University of Lorraine, Metz, France
*Corresponding author: e-mail address: benoit.beausir@univ-lorraine.fr

Contents

1. Introduction

1.1 Context and content of the chapter

After defining the working principle of the method in Chapter "Development of a homography-based global DIC approach for high-angular resolution in

Advances in Imaging and Electron Physics
ISSN 1076-5670
https://doi.org/10.1016/bs.aiep.2022.07.003

the SEM" by Ernould et al., its implementation is now detailed. For reminder, the present work was conducted as part of the first author's PhD thesis at the University of Lorraine from 2017 to 2020 (Ernould, 2020). It deals with the development of a high-angular resolution method for the measurement lattice rotations and elastic strains in the scanning electron microscope (Ernould, Beausir, Fundenberger, Taupin, & Bouzy, 2020a,c, 2021). This kind of technique is known as the HR-EBSD or, more recently, the HR-TKD technique, depending on whether it is applied to electron backscatter diffraction (EBSD) patterns or transmission Kikuchi diffraction (TKD) patterns. In the following, "HR-EBSD/TKD" will be used when no distinction is needed regarding the SEM-based configuration used.

Lattice rotations and elastic strains are deduced from the displacement field between two Kikuchi patterns belonging to the same crystal. To this end, a precise knowledge of the projection geometry is required (Britton et al., 2010; Villert, Maurice, Wyon, & Fortunier, 2009). In its original form, the HR-EBSD/TKD technique (Wilkinson, Meaden, & Dingley, 2006a,b) determines the displacement field from numerous local translation measurements. As discussed in Chapter "Measuring elastic strains and orientation gradients by scanning electron microscopy: Conventional and emerging methods" by Ernould et al. (sections 3 and 4.1), this approach uses a numerically efficient and relatively simple digital image correlation (DIC) algorithm, namely Fourier-transform based cross-correlation (FT-CC). It has been successfully applied to semi-conductors, but its performance decreases in the presence of a few degrees of disorientation, which is typical of deformed metals. Several improvements were consequently proposed. However, the method had also become more and more complex and crucial aspects of its implementation, such as the weighting of the local shift measurements, remain ambiguous in the literature.

Starting from general concepts of digital image registration techniques, a "global" approach is proposed as an alternative to the "local" HR-EBSD/TKD technique in Chapter "Development of a homography-based global DIC approach for high-angular resolution in the SEM" by Ernould et al. The displacement field between two diffraction patterns is captured using a unique and large region of interest. While the local approach considers solid square subsets, the present method accepts any shape and its relative deformations are modelled by a linear homography, which is a line but not edge preserving transformation. A linear homography perfectly

describes the theoretical displacement in the scintillator caused by the elastic deformation gradient tensor $\boldsymbol{F}^e$ as well as the effects of probe displacement. Its measurement is performed in spatial domain by means of an inverse-compositional Gauss-Newton (IC-GN) algorithm, i.e., an iterative local optimization scheme. The latter is standardly used, in particular in experimental mechanics.

This chapter details the implementation of the image registration procedure. First, it focuses on the IC-GN algorithm, for which the precomputed quantities are highlighted. Then, it explains how the IC-GN algorithm was modified to integrate a correction of optical distortions. Finally, an initial guess strategy based on global image cross-correlation techniques is proposed.

1.2 Reminder of notations and equations from previous chapters

1.2.1 Scintillator's frame

Let $\left(\overrightarrow{X_1}, \overrightarrow{X_2}, \overrightarrow{X_3}\right)$ be the scintillator's frame, whose axes $\overrightarrow{X_1}$ and $\overrightarrow{X_2}$ are aligned with the scintillator's horizontal and vertical edges, respectively. $\overrightarrow{X_1}$ is rightwards and $\overrightarrow{X_2}$ is downwards to be consistent with the usual matrix representation of images. For the sake of clarity, points belonging to the scintillator are denoted in two ways:

- Uppercase letters, $\boldsymbol{X}=[X_1 \;\; X_2]^T$, mean that absolute (or pixel) coordinates are considered. The origin is the upper left corner of the scintillator.
- Lowercase letters, $\boldsymbol{x}=[x_1 \;\; x_2]^T$, mean that relative coordinates with respect to pattern center (*PC*) are considered. The latter admits $\boldsymbol{X}^{PC}=\left[X_1^{PC} \;\; X_2^{PC}\right]^T$ for absolute coordinates, i.e., $x_i=X_i-X_i^{PC}$ $(i=1, 2)$.

1.2.2 Homography and homogeneous coordinates

A linear homography involves height deformation parameters h_{ij} stored in the deformation vector

$$\boldsymbol{p}=[\, h_{11} \;\; h_{12} \;\; h_{13} \;\; h_{21} \;\; h_{22} \;\; h_{23} \;\; h_{31} \;\; h_{32} \,]^T, \tag{1}$$

and commonly arranged in the shape function as follows (Baker & Matthews, 2004; Hartley & Zisserman, 2004):

$$\boldsymbol{W}(\boldsymbol{p}) = \begin{bmatrix} 1 + h_{11} & h_{12} & h_{13} \\ h_{21} & 1 + h_{22} & h_{23} \\ h_{31} & h_{32} & 1 \end{bmatrix}. \tag{2}$$

The shape function describes the transition from the reference (undeformed) subset to the deformed target subset, whose points $\boldsymbol{\xi}$ and $\boldsymbol{\xi}'$, respectively, are defined with respect to an arbitrary point X_0:

$$\boldsymbol{\xi}' = \boldsymbol{W}(\boldsymbol{p}).\boldsymbol{\xi}. \tag{3}$$

According to the aforementioned convention, the absolute coordinates of this arbitrary point are $\boldsymbol{X_0} = [X_{01} \quad X_{02}]^T$, while $\boldsymbol{x_0} = [x_{01} x_{02}]^T$ are its coordinates relative to the PC, i.e., $\boldsymbol{x_0} = \boldsymbol{X_0} - \boldsymbol{X}^{PC}$. As shown by red vectors in Fig. 1, the coordinates of $\boldsymbol{\xi}$ and $\boldsymbol{\xi}'$ are the same, no matter they are computed from the points' absolute coordinates, $\boldsymbol{\xi} = \boldsymbol{X} - \boldsymbol{X_0}$ and $\boldsymbol{\xi}' = \boldsymbol{X}' - \boldsymbol{X_0}$ (Fig. 1A), or from its relative coordinates, $\boldsymbol{\xi} = \boldsymbol{x} - \boldsymbol{x_0}$ and $\boldsymbol{\xi}' = x' - \boldsymbol{x_0}$.

The parametrization of the homography in Eq. (2) describes a two-dimensional transformation in the plane $\left(\overrightarrow{X_1}, \overrightarrow{X_2}\right)$, but $\boldsymbol{\xi}$ and $\boldsymbol{\xi}'$ are three-components vector in Eq. (3). This is because homogeneous coordinates are considered. A 2-dimensionnal vector has unique Euclidean coordinates, $\boldsymbol{\xi} = [e_1 \quad e_2]^T$ but it can be represented by an infinity of possible three-dimensional vectors $\boldsymbol{\xi} = [h_1 \quad h_2 \quad h_3]^T$ where ${h_1}^2 + {h_2}^2 + {h_3}^2 \neq 0$ when using homogeneous coordinates. Specifically, an important property of homogeneous coordinates is:

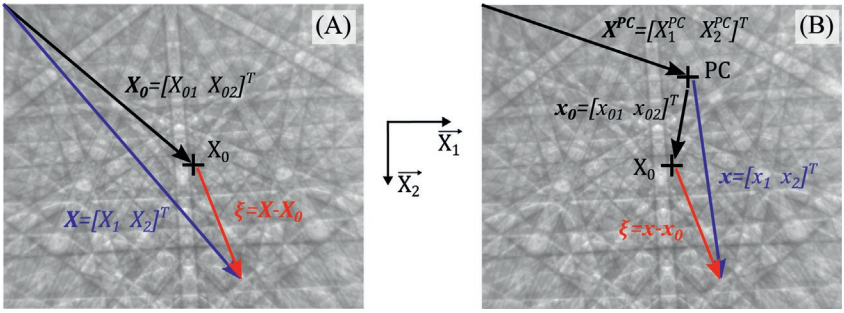

Fig. 1 Definition of the position within the reference subset $\boldsymbol{\xi}$ (A) from the points' absolute coordinates or (B) from their coordinates relative to the PC.

$$\forall \lambda \in \mathbb{R}^*,\ \boldsymbol{\xi} = \lambda.\boldsymbol{\xi}. \tag{4}$$

When the last component in 1 in homogeneous coordinates, then other components equal the Euclidean ones. In the present example, provided $h_3 \neq 0$, it arises $h_1/h_3 = e_1$ and $h_2/h_3 = e_2$ since $\boldsymbol{\xi} = (1/h_3).\ \boldsymbol{\xi} = [h_1/h_3 \quad h_2/h_3 \quad 1]^T$ according to Eq. (4).

1.2.3 Similarity criterion and IC-GN algorithm

The IC-GN algorithm determines the deformation parameters of the homography, denoted h_{ij}, which ensure the highest similarity between the reference and the target patterns. To this purpose, it iteratively computes the deformation increment $\boldsymbol{\Delta p}$ minimizing the similarity criterion C^{IC}_{ZNSSD} in the neighborhood of the current estimate $\boldsymbol{p}$ of the solution:

$$C^{IC}_{ZNSSD}(\boldsymbol{\Delta p}) = \sum_{i=1}^{N}\left[\frac{R\left(\boldsymbol{W}\left(\boldsymbol{X}^{(i)},\ \boldsymbol{\Delta p}\right)\right) - \overline{r}}{\Delta\widetilde{r}} - \frac{T\left(\boldsymbol{W}\left(\boldsymbol{X}^{(i)},\ \boldsymbol{p}\right)\right) - \overline{t}}{\Delta\widetilde{t}}\right]^2 \tag{5}$$

$$\overline{r} = \frac{1}{N}\sum_{i=1}^{N} R\left(\boldsymbol{W}\left(\boldsymbol{X}^{(i)}, \boldsymbol{\Delta p}\right)\right) \qquad \Delta\widetilde{r} = \sqrt{\sum_{i=1}^{N}\left[R\left(\boldsymbol{W}\left(\boldsymbol{X}^{(i)}, \boldsymbol{\Delta p}\right)\right) - \overline{r}\right]^2}$$

$$\overline{t} = \frac{1}{N}\sum_{i=1}^{N} T\left(\boldsymbol{W}\left(\boldsymbol{X}^{(i)}\boldsymbol{p}\right)\right) \qquad \Delta\widetilde{t} = \sqrt{\sum_{i=1}^{N}\left[T\left(\boldsymbol{W}\left(\boldsymbol{X}^{(i)}\boldsymbol{p}\right)\right) - \overline{t}\right]^2}.$$

The C^{IC}_{ZNSSD} criterion is the zero-mean normalized sum of squared differences (ZNSSD) in the intensities of the reference subset r and the target subset t, formed of N points of absolute location $\boldsymbol{X}$ in the reference R and target T patterns. During each iteration of the IC-GN algorithm, the target subset is warped by $\boldsymbol{p}$ and remains fixed, while the reference subset is initially undeformed and experiences an incremental warping by $\boldsymbol{\Delta p}$. To compute this increment, the Gauss-Newton algorithm linearizes the similarity criterion by taking the Taylor series expansion to order 1 of the function R in the neighborhood of $\boldsymbol{p} = \boldsymbol{0}$:

$$R\left(\boldsymbol{W}\left(\boldsymbol{X}^{(i)},\ \boldsymbol{\Delta p}\right)\right) \approx R\left(\boldsymbol{X}^{(i)}\right) + \left[\boldsymbol{\nabla R}\left(\boldsymbol{X}^{(i)}\right)\right]^T.\frac{\partial \boldsymbol{W}}{\partial \boldsymbol{p}}\left(\boldsymbol{\xi}^{(i)}, \boldsymbol{0}\right).\boldsymbol{\Delta p} \tag{6}$$

After each iteration, the solution is updated using an inverse-compositional scheme,

$$\boldsymbol{W}(\boldsymbol{p}) \leftarrow \boldsymbol{W}(\boldsymbol{p}) \circ \boldsymbol{W}^{-1}(\Delta \boldsymbol{p}), \tag{7}$$

so that only the target subset is deformed at the beginning of each iteration.

2. Standard implementation of the IC-GN algorithm

Note that this section is mainly based on the implementation of the IC-GN algorithm described by (Blaber, Adair, & Antoniou, 2015) in the open-source software Ncorr. The latter considers an affine shape function. Here, formula are adapted to a linear homography.

2.1 Pre-computed quantities

As detailed in Chapter "Development of a homography-based global DIC approach for high-angular resolution in the SEM" by Ernould et al. (section 4.2), the IC-GN algorithm has a higher numerical efficiency than the forward-additive Gauss-Newton (FA-GN) since the Taylor series expansion in Eq. (6) does not depend on the current estimate of the solution. Therefore, several quantities like the Hessian matrix $\boldsymbol{H}$ are precomputable, as shown in yellow highlights in Fig. 2.

The undeformed reference subset composed of the N points of absolute coordinates $\boldsymbol{X}^{(i)}$ is extracted from the reference pattern of intensity R. The subset's intensities are zero-mean normalized as follows:

$$r\left(\boldsymbol{\xi}^{(i)}\right) = \frac{R\left(\boldsymbol{X}^{(i)}\right) - \overline{r}}{\Delta\widetilde{r}} \tag{8}$$

where $\overline{r}$ is the mean intensity of the raw subset,

$$\overline{r} = \frac{1}{N}\sum_{i=1}^{N} R\left(\boldsymbol{X}^{(i)}\right), \tag{9}$$

and where,

$$\Delta\widetilde{r} = \sqrt{\sum_{i=1}^{N}\left[R\left(\boldsymbol{X}^{(i)}\right) - \overline{r}\right]^2}, \tag{10}$$

is the square root of the zero-mean subset's variance multiplied by $\sqrt{N-1}$. As highlighted in Fig. 2, $r(\boldsymbol{\xi}^{(i)})$ and $\Delta\widetilde{r}$ are stored for future use. Points forming the subset are identified form their location $\boldsymbol{\xi}^{(i)} = \boldsymbol{X}^{(i)} - \boldsymbol{X}_{\boldsymbol{0}}$.

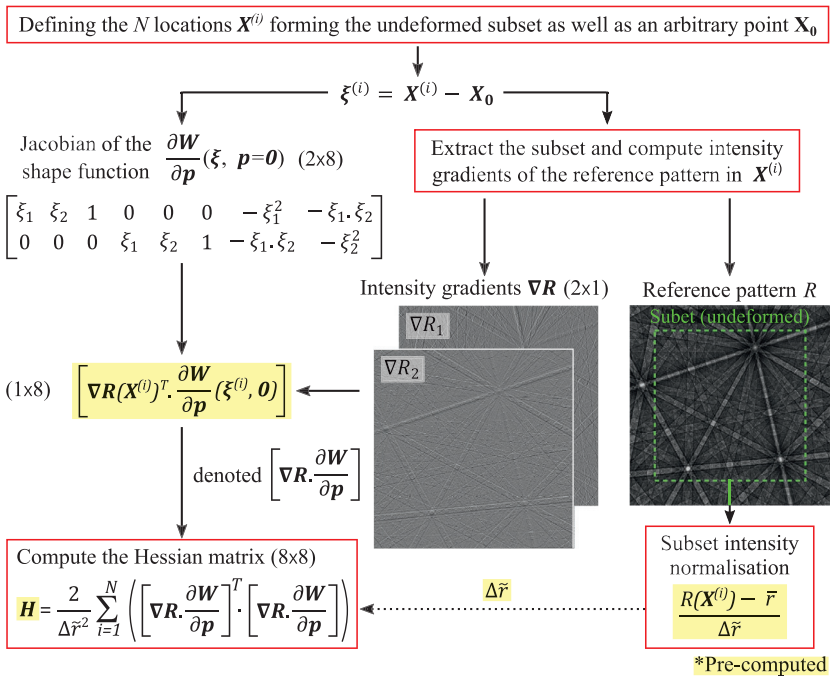

Fig. 2 Steps involved in calculating the pre-computable quantities of the IC-GN algorithm.

The arbitrary reference $\boldsymbol{X_0}$ is typically the geometric center of the subset, so that $\boldsymbol{\xi}^{(i)}$ is defined independently from any consideration regarding the projection geometry. On the contrary, integrated DIC approaches for HR-EBSD/TKD (Ruggles, Bomarito, Qiu, & Hochhalter, 2018; Shi, Roux, Latourte, & Hild, 2019; Vermeij & Hoefnagels, 2018) (see section 4.2 in Chapter "Measuring elastic strains and orientation gradients by scanning electron microscopy: Conventional and emerging methods" by Ernould et al.) rather make it coincide with the pattern center $\boldsymbol{X^{PC}}$, so that $\boldsymbol{\xi}^{(i)} = \boldsymbol{x}^{(i)}$.

The intensity gradients of the reference pattern at location $\boldsymbol{X}^{(i)}$ (2×1),

$$\boldsymbol{\nabla R}\left(\boldsymbol{X}^{(i)}\right) = \begin{bmatrix} \nabla R_1\left(\boldsymbol{X}^{(i)}\right) \\ \nabla R_2\left(\boldsymbol{X}^{(i)}\right) \end{bmatrix}, \tag{11}$$

can be computed in different ways. Following (Blaber et al., 2015), intensity gradients are here derived from the biquintic B-splines coefficients. By using splines coefficients, intensity gradients can be easily interpolated if non-integer coordinates $\boldsymbol{\xi}^{(i)}$ are considered. This is of particular interest to integrate a correction of optical distortions as detailed in Section 3.

The Jacobian of the shape function $\partial \boldsymbol{W}/\partial \boldsymbol{p}$ is evaluated for $\boldsymbol{p}=\boldsymbol{0}$ at each $\boldsymbol{\xi}^{(i)}$ location. The parametrization of the homography has to be differentiable with respect to $\boldsymbol{p}$ and invertible. Note that the second condition is specific to the IC-GN algorithm because of Eq. (7). It is not necessary for a forward-additive approach. The parametrization in Eq. (2) fulfills both conditions and the Jacobian is computed by deriving

$$\xi_i' = \frac{(1+h_{i1}).\xi_1 + h_{i2}.\xi_2 + h_{i3}}{h_{31}.\xi_1 + h_{32}.\xi_2 + 1} \tag{12}$$

where $i=1, 2$, which is obtained using Eq. (3). Thus, $\partial \boldsymbol{W}/\partial \boldsymbol{p}$ is a (2×8)-matrix:

$$\frac{\partial \boldsymbol{W}}{\partial \boldsymbol{p}}(\boldsymbol{\xi}, \boldsymbol{p}) = \frac{1}{h_{31}.\xi_1 + h_{32}.\xi_2 + 1}\begin{bmatrix} \xi_1 & \xi_2 & 1 & 0 & 0 & 0 & -\xi_1.\xi_1' & -\xi_2.\xi_1' \\ 0 & 0 & 0 & \xi_1 & \xi_2 & 1 & -\xi_1.\xi_2' & -\xi_2.\xi_2' \end{bmatrix} \tag{13}$$

where $\boldsymbol{\xi}=\begin{bmatrix}\xi_1 & \xi_2 & 1\end{bmatrix}^T$ is chosen as a possible representation in homogeneous coordinates of $\boldsymbol{\xi}=\begin{bmatrix}X_1-X_{01} & X_2-X_{02}\end{bmatrix}^T$ in Euclidean coordinates ($\xi_i=X_i-X_{0i}$ since the third homogeneous coordinate is 1). Considering $\boldsymbol{p}=\boldsymbol{0}$, Eq. (13) yields:

$$\frac{\partial \boldsymbol{W}}{\partial \boldsymbol{p}}(\boldsymbol{\xi}, \boldsymbol{0}) = \begin{bmatrix} \xi_1 & \xi_2 & 1 & 0 & 0 & 0 & -\xi_1^2 & -\xi_1.\xi_2 \\ 0 & 0 & 0 & \xi_1 & \xi_2 & 1 & -\xi_1.\xi_2 & -\xi_2^2 \end{bmatrix}. \tag{14}$$

The intensity gradients and the Jacobian are multiplied and the so obtained matrix (1×8) is denoted $[\boldsymbol{\nabla R}.\,\partial \boldsymbol{W}/\partial \boldsymbol{p}]$ in the following. In practice, the latter is computed for each point of the subset, resulting in an $(8\times N)$ matrix, the i-th line of which being associated with $\boldsymbol{\xi}^{(i)}$. This matrix is saved for future use.

Once all the aforementioned computations are performed, the Hessian matrix is finally obtained:

$$\boldsymbol{H} = \frac{2}{\Delta\widetilde{r}^2}\sum_{i=1}^{N}\left(\left[\boldsymbol{\nabla R}.\frac{\partial \boldsymbol{W}}{\partial \boldsymbol{p}}\right]^T.\left[\boldsymbol{\nabla R}.\frac{\partial \boldsymbol{W}}{\partial \boldsymbol{p}}\right]\right). \tag{15}$$

As detailed in (Blaber et al., 2015), this relationship involves several simplifying assumptions intrinsic to the Gauss-Newton algorithm. The quantities $\overline{r}$ and $\Delta\widetilde{r}$ are assumed to be unchanged when the reference subset is deformed by the increment $\boldsymbol{\Delta p}$. The current estimate $\boldsymbol{p}$ must be close to the solution.

2.2 Algorithm's workflow

The workflow of the IC-GN algorithm is illustrated in Fig. 3, where the previously precomputed quantities are in yellow highlights.

At the beginning of the algorithm, the target subset is pre-aligned with respect to the reference subset by deforming it according to the

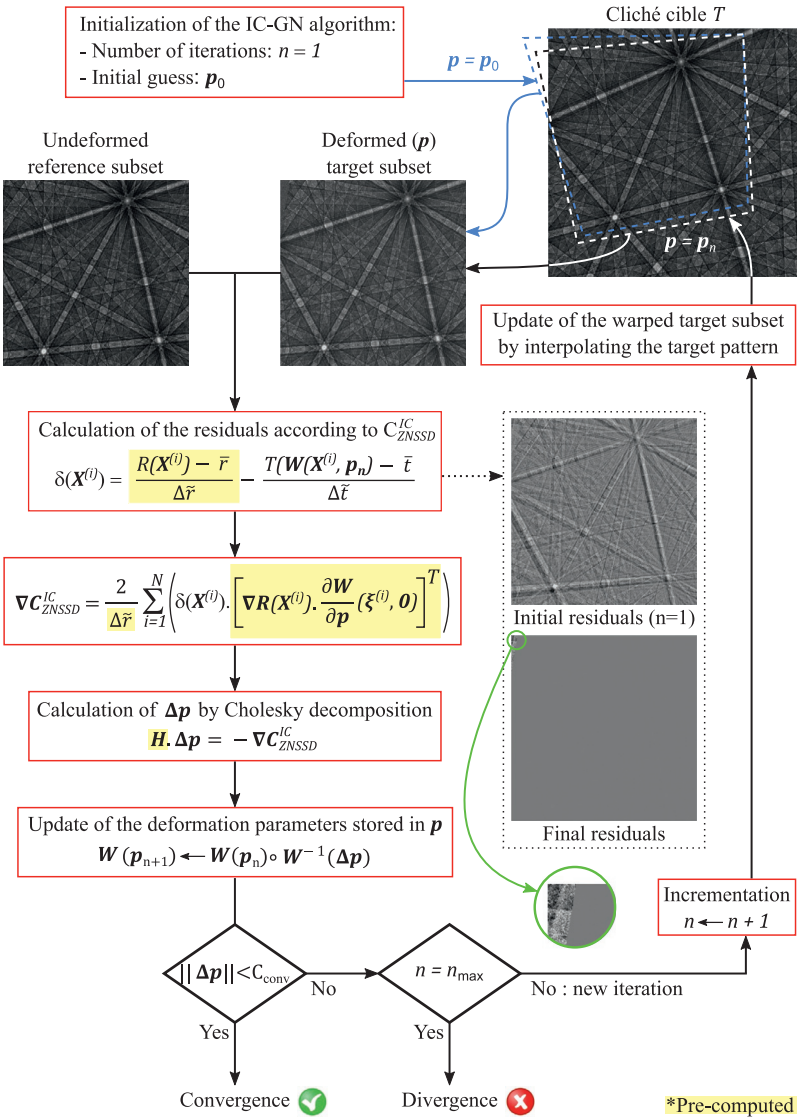

Fig. 3 Workflow of the IC-GN algorithm.

initial guess $\boldsymbol{p_0}$. The target subset at the beginning of the first iteration is thus constructed by interpolating the target pattern T in $\boldsymbol{X'^{(i)}} = \boldsymbol{X_0} + \boldsymbol{\xi'^{(i)}}$ where

$$\boldsymbol{\xi'^{(i)}} = \boldsymbol{W}(\boldsymbol{p_0}).\boldsymbol{\xi^{(i)}} = \boldsymbol{W}\left(\boldsymbol{X^{(i)}}, \boldsymbol{p_0}\right). \tag{16}$$

It corresponds to the region delimited by a blue dotted line in the target pattern in Fig. 3. In case the position to interpolate lies outside the image, noise is introduced.

Regarding the core of the algorithm, the following steps are performed at each iteration:

(1) Intensities of the warped target subset are zero-mean normalized like already described in Section 2.1 regarding the reference subset.

(2) The residuals δ, i.e., the differences in intensity between the reference and the target subsets,

$$\delta\left(\boldsymbol{X^{(i)}}\right) = \frac{R\left(\boldsymbol{X^{(i)}}\right) - \overline{r}}{\Delta\widetilde{r}} - \frac{T\left(\boldsymbol{W}\left(\boldsymbol{X^{(i)}}, \boldsymbol{p_n}\right)\right) - \overline{t}}{\Delta\widetilde{t}}, \tag{17}$$

are computed and stored in a vector of size N. The algorithm minimizes these residuals, which are ideally zero after image registration. This is suggested in Fig. 3, where the final residuals are almost all zero. Only the upper left corner of the subset has notable residuals (circled in green). They are due to noise introduced for points outside the target pattern.

(3) The gradient of the correlation criterion (8×1),

$$\boldsymbol{\nabla C^{IC}_{ZNSSD}} = \frac{2}{\Delta\widetilde{r}} \sum_{i=1}^{N} \left(\delta\left(\boldsymbol{X^{(i)}}\right).\left[\boldsymbol{\nabla R}.\frac{\partial \boldsymbol{W}}{\partial \boldsymbol{p}}\right]\right), \tag{18}$$

is calculated by performing the matrix product of the array of size $8 \times N$ storing the pre-computed $[\boldsymbol{\nabla R}.\,\partial \boldsymbol{W}/\partial \boldsymbol{p}]$ values with the vector of the residuals.

(4) The deformation increment $\boldsymbol{\Delta p}$ is solved by Cholesky decomposition of the following equation:

$$\boldsymbol{H}.\boldsymbol{\Delta p} = -\boldsymbol{\nabla C^{IC}_{ZNSSD}}. \tag{19}$$

(5) The deformation parameters of the homography are updated using the inverse-compositional scheme in Eq. (7).

(6) Convergence is achieved when the norm of the increment $\boldsymbol{\Delta p}$ is less than the convergence criterion C_{conv}. Otherwise, the algorithm iterates by updating the target subset from the new evaluation of the deformation parameters, unless the maximum number of allowed iterations n_{max} is reached. If so, the algorithm diverges. The norm of $\boldsymbol{\Delta p}$ is defined as follows:

$$||\boldsymbol{\Delta p}|| = \sqrt{\sum_{i=1}^{3}\left(\left(\xi_{1max}.\Delta h_{i1}\right)^2 + \left(\xi_{2max}.\Delta h_{i2}\right)^2\right) + \Delta h_{13}^2 + \Delta h_{23}^2} \quad (20)$$

where $\xi_{1max} = \max|\xi_1^{(i)}|$ and $\xi_{2max} = \max|\xi_2^{(i)}|$ where $i \in [\![1, N]\!]$. This definition is inspired by (Pan, Li, & Tong, 2013), who consider an affine shape function. The convergence criterion C_{conv} is set to 0.001 pixel. This value is commonly used in the literature (Pan et al., 2013; Shao, Dai, & He, 2015; Zhang et al., 2015) and agrees with the recommendation in (Pan, 2014), namely $C_{conv} \leq 0.01$. The relevance of this value will be checked during the numerical validation of the method in the next chapter ("Numerical validation and influence of optical distortions on accuracy" by Ernould et al.).

3. Modified IC-GN algorithm to integrate a correction of optical distortions

As discussed in Chapter "Measuring elastic strains and orientation gradients by scanning electron microscopy: Conventional and emerging methods" by Ernould et al. (section 3.3), camera lenses generate optical distortions that disturb the displacement field sought by the HR-EBSD/TKD technique. Until present, Kikuchi patterns were pre-processed to remove distortion effects like in (Maurice, Dzieciol, & Fortunier, 2011; Shi et al., 2019) for instance. This section details the integration of a correction in the IC-GN algorithm to avoid this step. The impact of such a correction on the algorithm's execution speed is also assessed.

3.1 Correction's working principle

As shown Fig. 4, the homography assumption is valid on the scintillator (top of the figure). However, the composition of the distortion model D of the camera's optics and the homography is observed on the Kikuchi patterns (bottom of the figure).

The IC-GN algorithm considers a region of interest in a "virtually" undistorted configuration. The proposed correction deals as an interface between the latter and the actual (distorted) images to be registered, as illustrated in Fig. 5. It consists of a distortion model D defining, for each point $\boldsymbol{X}^{(i)}$ or $\boldsymbol{X'}^{(i)}$ ($i \in [\![1, N]\!]$) in the undistorted configuration, its associated position $\widetilde{\boldsymbol{X}}^{(i)}$ or $\widetilde{\boldsymbol{X}}\boldsymbol{I}^{(i)}$ in the distorted configuration, i.e., $\widetilde{\boldsymbol{X}}^{(i)} = D\left(\boldsymbol{X}^{(i)}\right)$ et $\widetilde{\boldsymbol{X}}\boldsymbol{I}^{(i)} = D\left(\boldsymbol{X}\boldsymbol{I}^{(i)}\right)$. The IC-GN algorithm is implemented as described in

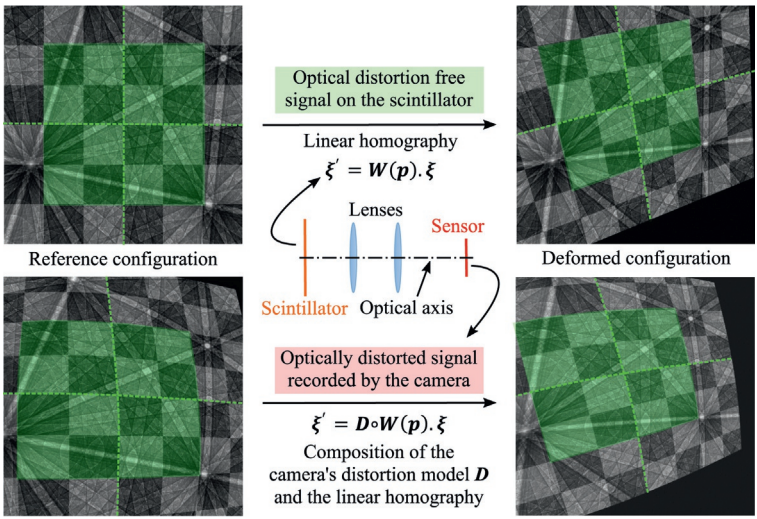

Fig. 4 Comparison of (top) a homography occurring in the scintillator and (bottom) the transformation actually recorded by the camera sensor in the case its optics cause radial distortion (exaggerated here).

Section 2, except that any interpolation of the image intensity or intensity gradients at $\boldsymbol{X}^{(i)}$ or $\boldsymbol{X}'^{(i)}$ (green dots in Fig. 4) is actually performed at $\widetilde{\boldsymbol{X}}^{(i)}$ or $\widetilde{\boldsymbol{X}}\boldsymbol{I}'^{(i)}$ (blue dots in Fig. 4), respectively.

Concretetely, $\boldsymbol{\xi}^{(i)}$ locations remain unchanged as they are associated to the virtually undistored space as shown in the top of Fig. 5. The Jacobian of the shape function in Eq. (14) is therefore the same but it is no longer multiplied by the intensity gradients of the reference image at $\boldsymbol{X}^{(i)}$, but at $\widetilde{\boldsymbol{X}}^{(i)}$ in Eq. (11). Similarly, $\boldsymbol{X}^{(i)}$ and $\boldsymbol{X}'^{(i)}$ are substituted by $\widetilde{\boldsymbol{X}}^{(i)}$ and $\widetilde{\boldsymbol{X}}\boldsymbol{I}'^{(i)}$ in Eq. (17), respectively. Once the deformation parameters of the homography are measured, the solution is deduced analytically by considering the coordinates of the PC and its possible displacement in the undistorted configuration. Note that formula with $\widetilde{\boldsymbol{X}}^{(i)}$ and $\widetilde{\boldsymbol{X}}\boldsymbol{I}'^{(i)}$ are available in (Ernould et al., 2021). They are not rewritten here for the sake of brevity.

In practice, the distortion model and its parameters depend on each camera. Like any model, it is a simplified and more or less faithful description of reality. The choice of a suitable distortion model D and the determination of the values of its coefficients are the responsibility of the user. If the user is free in the choice of the model, the operating principle of the correction nevertheless supposes that:

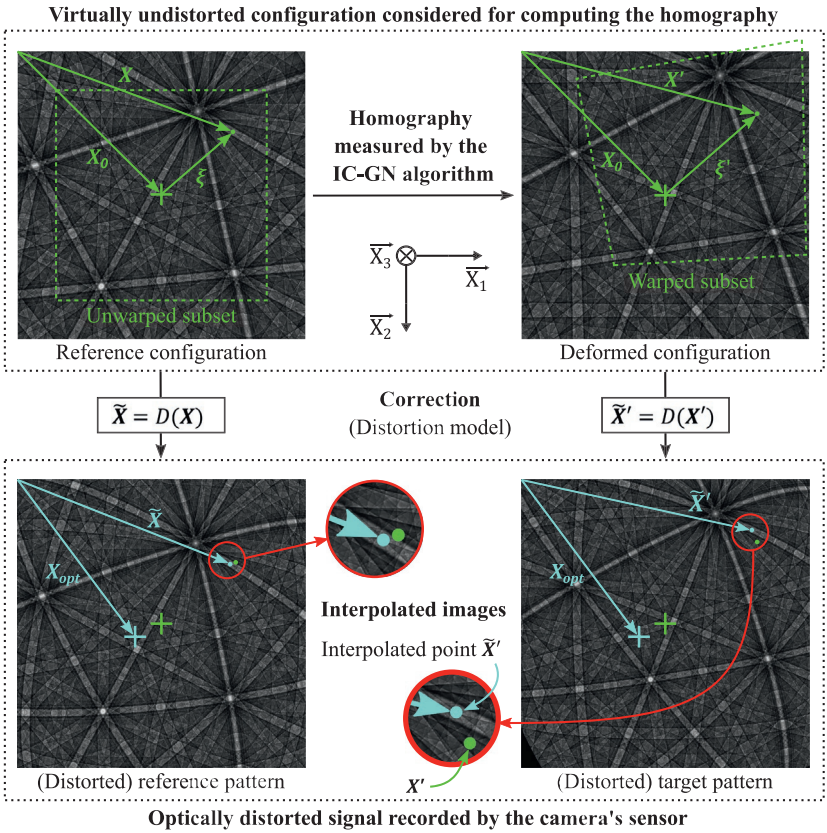

Fig. 5 Working principle of the optical distortion correction integrated in the Gauss-Newton algorithm. The homography is measured by considering undistorted images and each time an interpolation is required (green dots), the distortion model D corrects the position to be interpolated in the real distorted images (blue dots).

(i) The distortion model D depends exclusively on the position $\boldsymbol{X}^{(i)}$ or $\boldsymbol{X}'^{(i)}$ in the undistorted configuration.

(ii) The target and reference patterns are affected equally by optical distortions.

The former is verified by the most common models (Tang, Grompone von Gioi, Monasse, & Morel, 2017; Wang, Shi, Zhang, & Liu, 2008) while the latter is acceptable for a dataset acquired with the same camera. Some precautions should be taken, such as turning on the camera one to two hours before the start of the acquisition. Indeed, optical distortions can vary over time due to the self-heating of the camera components, especially its photographic sensor (Ma, Pang, & Ma, 2012).

3.2 Impact of the correction on the execution speed of the IC-GN

The numerical extra cost of the correction was evaluated by comparing the execution time of the IC-GN algorithm with and without correction. To do so, 20,000 iterations were performed with a reset of the deformation parameters at the beginning of each iteration. Each iteration was thus identical. Intermediate execution times were recorded every 1000 iterations to verify that the execution speed is relatively constant. This was the case since no deviation of more than 2% from the average was observed.

The Brown-Conrady model (Brown, 1966, 1971; Conrady, 1919) was used to describes radial and tangential distortions up to third order, through the distortion coefficients K_i and P_i ($i \in [\![1,3]\!]$), respectively:

$$\begin{pmatrix} \widetilde{X}_1 \\ \widetilde{X}_2 \end{pmatrix} = \begin{pmatrix} X_1 \\ X_2 \end{pmatrix} + \underbrace{\left(K_1.r^2 + K_2.r^4 + K_3.r^6\right).\begin{pmatrix} \Delta_1 \\ \Delta_2 \end{pmatrix}}_{\text{Radial distortion}} + \underbrace{\left(1 + P_3.r^2\right).\begin{pmatrix} P_1.\left(r^2 + 2.\Delta_1^2\right) + 2.P_2.\Delta_1.\Delta_2 \\ P_2.\left(r^2 + 2.\Delta_2^2\right) + 2.P_1.\Delta_1.\Delta_2 \end{pmatrix}}_{\text{Tangential distortion}} \tag{21}$$

where $\Delta_i = X_i - X_i^{opt}$ ($i = 1, 2$), $r = \sqrt{\Delta_1^2 + \Delta_2^2}$ and $\boldsymbol{X_{opt}} = \left[X_1^{opt}\ X_2^{opt}\right]^T$ are the absolute coordinates of the optical center.

This model was chosen since it is widely used. For instance, a simplified version of this model was considered by (Mingard, Day, Maurice, & Quested, 2011) to calibrate several EBSD cameras, as well as by (Britton et al., 2010), to assess the error of the local HR-EBSD/TKD technique when neglecting distortion effects (see section 3.3.2 and fig. 14 in Chapter "Measuring elastic strains and orientation gradients by scanning electron microscopy: Conventional and emerging methods" by Ernould et al.). Here, third order distortions were accounted for, to make the model relatively complex. This tends to overestimate the extra cost of the correction as compared to more practical cases. This is also a fairer approach given an optimization of the code (apart from the correction) is always possible.

As a result, the correction increased the runtime by ~6.2% when the target image was interpolated using biquintic B-splines, for which the 36 coefficients were pre-computed. The experiment was repeated with a

bicubic interpolation for which the 16 interpolation coefficients were also pre-computed, which led to a runtime increased by ~8.2%. This value is higher because this second interpolation scheme is simpler. The overall numerical cost of the algorithm decreases while the correction cost remains unchanged. Therefore, the correction is not expected to lengthen the analysis time by more than 10%, especially since the use of a high-order interpolation scheme is recommended for accuracy (Pan, 2018).

4. Global cross-correlation based initial guess strategy

As detailed in Chapter "Measuring elastic strains and orientation gradients by scanning electron microscopy: Conventional and emerging methods" by Ernould et al. (section 4.2.2), the IC-GN algorithm needs an initial guess of the solution to converge efficiently. If the estimate is too far from the true solution, the algorithm may converge to a local optimum of the similarity criterion, not the global one, or even diverge. In this section, already proposed initial guess strategies for global HR-EBSD/TKD approaches are first briefly discussed, and an alternative one is then suggested. The latter pre-aligns diffraction patterns by means of Fourier-Mellin transform and Fourier-transform based cross-correlation.

4.1 Choice of the initial guess strategy

4.1.1 Overview of the already proposed strategies

Generally speaking, initial guess strategies are either independent or dependent on the order in which the points are analyzed (path independent or path dependent) (Pan, 2018). In the context of the HR-EBSD/TKD technique, points refer to pixels of the orientation map.

Regarding the strategies already proposed in the literature, indexing-based initialization (Ruggles et al., 2018; Vermeij & Hoefnagels, 2018) belongs to the former category. Such an approach was initially by published by (Maurice, Driver, & Fortunier, 2012) as part of the remapping technique of the local HR-EBSD/TKD technique (see Chapter "Measuring elastic strains and orientation gradients by scanning electron microscopy: Conventional and emerging methods" by Ernould et al., section 3.2.2). The relative rotations between the reference and the target patterns are deduced from the local crystal orientations, so that the solution is a priori known, within the indexing error and elastic deformation.

A path-dependent strategy was applied by (Shi et al., 2019). They initialized a point near the reference with the identity matrix, and then used

the obtained solution to initialize adjacent points. Their approach has the advantage of being fast because it does not require specific calculations. However, the order in which the points are processed is crucial for the success of the analysis, as errors can be propagated. A reliability-guided strategy can reduce that risk (Pan, 2009). The choice of the neighbor for the initialization, and thus the order of processing of the points, is based on those which have the best correlation with the reference. Despite this, such a strategy may be flawed in plastically deformed materials due to discontinuities that may be constituted, for example, by sub-grain boundaries.

Hybrid strategies are of course possible and even recommended (Pan, 2018) to benefit from the low computational effort of a path-dependent initialization while using a path-independent one if discontinuities or unreliability are detected.

4.1.2 Implementation of an initialization from Euler angles

The homography can be estimated from the Euler angles as follows:

(1) Estimation of the three rotations w_i^{index} (exponent "index" for "indexing") with respect to the axes $\overrightarrow{X_i^S}$ of the sample frame S, which describe the transition from the reference to the deformed configurations.

(2) Composition of the three rotations w_i^{index} to deduce the global rotation matrix $\boldsymbol{R^S}$, expressed in the sample frame:

$$\begin{aligned}\boldsymbol{R^S} &= \boldsymbol{R_3^S}.\boldsymbol{R_2^S}.\boldsymbol{R_1^S} \\ &= \begin{bmatrix} c_3 & -s_3 & 0 \\ s_3 & c_3 & 0 \\ 0 & 0 & 1 \end{bmatrix}.\begin{bmatrix} c_2 & 0 & s_2 \\ 0 & 1 & 0 \\ -s_2 & 0 & c_2 \end{bmatrix}.\begin{bmatrix} 1 & 0 & 0 \\ 0 & c_1 & -s_1 \\ 0 & s_1 & c_1 \end{bmatrix}.\end{aligned} \tag{22}$$

where $c_i = \cos(w_i^{index})$ et $s_i = \sin(w_i^{index})$, $i \in [\![1;3]\!]$, hence:

$$\boldsymbol{R^S} = \begin{bmatrix} c_2.c_3 & s_1.s_2.c_3 - c_1.s_3 & c_1.s_2.c_3 + s_1.s_3 \\ c_2.s_3 & s_1.s_2.s_3 + c_1.c_3 & c_1.s_2.s_3 - s_1c_3 \\ -s_2 & s_1.c_2 & c_1.c_2 \end{bmatrix}. \tag{23}$$

(3) Change of basis from the sample to the detector frame (exponent R for "registration"):

$$\boldsymbol{R^R} = \boldsymbol{P_R^S}.\boldsymbol{R^S}.\boldsymbol{P_S^R} \tag{24}$$

where $\boldsymbol{P_R^S}$ is the transition matrix from the scintillator frame to the sample frame, and conversely, $\boldsymbol{P_S^R} = (\boldsymbol{P_R^S})^{-1}$ is the transition matrix from the sample to the detector. Note that $(\boldsymbol{P_R^S})^{-1} = (\boldsymbol{P_R^S})^T$ since they are rotation matrices.

(4) Initialization of the deformation parameters h_{ij} of the homography by considering the components $\widehat{R}_{ij}^{R} = R_{ij}^{R}/R_{33}^{R}$ instead of those of $\widehat{\boldsymbol{F}}^{e}$ in Eq. (16) in Chapter "Development of a homography-based global DIC approach for high-angular resolution in the SEM" by Ernould et al., i.e.:

$$\begin{bmatrix} h_{11} & h_{12} & h_{13} \\ h_{21} & h_{22} & h_{23} \\ h_{31} & h_{32} & 1 \end{bmatrix} = \frac{1}{\gamma_0} \begin{bmatrix} \gamma_{11} & DD.\widehat{R}_{12}^{R} - \widehat{R}_{32}^{R}.x_{01} & \gamma_{13} \\ DD.\widehat{R}_{21}^{R} - \widehat{R}_{31}^{R}.x_{02} & \gamma_{22} & \gamma_{23} \\ \widehat{R}_{31}^{R} & \widehat{R}_{32}^{R} & 1 \end{bmatrix} \tag{25}$$

where $\gamma_0 = DD + \widehat{R}_{31}^{R}.x_{01} + \widehat{R}_{32}^{R}.x_{02}$

$$\gamma_{11} = DD.\widehat{R}_{11}^{R} - \widehat{R}_{31}^{R}.x_{01} - \gamma_0$$

$$\gamma_{22} = DD.\widehat{R}_{22}^{R} - \widehat{R}_{32}^{R}.x_{02} - \gamma_0$$

$$\gamma_{13} = DD.\left[\left(\widehat{R}_{11}^{R} - 1\right).x_{01} + \widehat{R}_{12}^{R}.x_{02} + \widehat{R}_{13}^{R}.DD\right] + x_{01}.(DD - \gamma_0)$$

$$\gamma_{23} = DD.\left[\widehat{R}_{21}^{R}.x_{01} + \left(\widehat{R}_{22}^{R} - 1\right).x_{02} + \widehat{R}_{23}^{R}.DD\right] + x_{02}.(DD - \gamma_0).$$

4.1.3 Alternative method based on global image cross-correlation

In the present work, most Kikuchi patterns were indexed by the BRUKER Esprit 1.9 software where the resolution of the Hough-transform was set to maximum. However, an initialization based on Euler angles often yield unsatisfactory results. Fig. 6A shows the intra-granular disorientation angle deduced from indexing in an IF (interstitial free) steel after 15% tensile deformation. When used as an initial guess, outliers are locally obtained, as highlighted by red circles in Fig. 6B. They result from the divergence of the IC-GN algorithm. Consequently, an alternative initialization had to be considered.

Grain internal disorientations are very often below 15°, this value being typically set as a tolerance for grain detection. For such a range of disorientation, the effects of rotations can be roughly visualized as translation and in-plane rotation of the Kikuchi patterns as shown in Fig. 7. Based on this, a method inspired by the one by (Pan, Wang, & Tian, 2017), which pre-aligns speckles patterns subject to a relative shift, scale and in-plane rotation, was developed

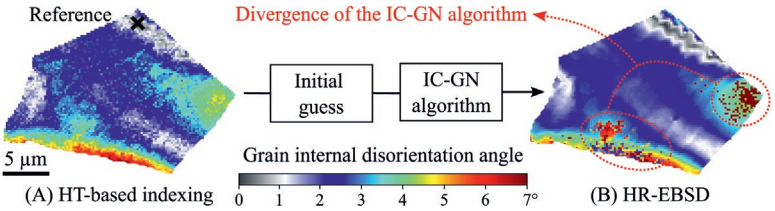

Fig. 6 IF steel grain characterized by EBSD. (A) Grain internal disorientation angle from Hough-transform (HT) based indexing by BRUKER Esprit 1.9 software. (B) Disorientation angle determined by HR-EBSD when the homography is initialized from Euler angles. Note that this example is extracted from a dataset that will be studied in Chapter "Applications of the method" by Ernould et al.

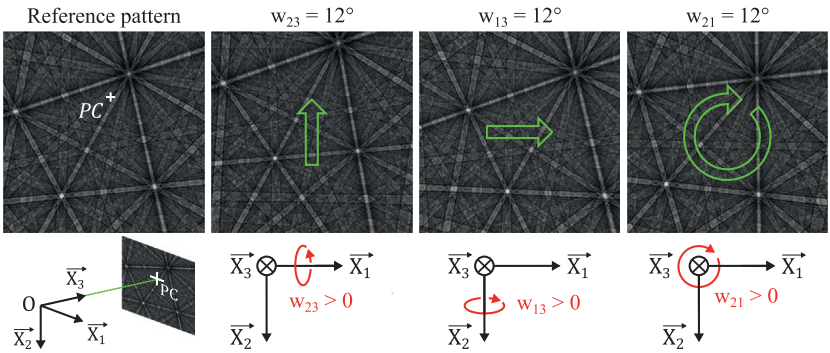

Fig. 7 Effect of a rotation around an axis of the scintillator frame.

The proposed initial guess strategy relies on global image cross-correlation. One large square subset is extracted from the reference pattern and the target pattern. Both subsets are first pretreated, in a manner quite similar to what is done by the local HR-EBSD/TKD approach, as will be detailed in Section 4.2.1. Then, they are pre-aligned following these four main steps, which are also illustrated in Fig. 8:

(1) In-plane rotation angle θ_0 (around $\overrightarrow{X_3}$) of the target pattern relative to the reference pattern is estimated by means of Fourier-Mellin transform based cross-correlation (FMT-CC) applied to a large and unique square subset. This step is detailed in Section 4.2.2.

(2) The target subset is rotated by $-\theta_0$ with respect to its geometric center.

(3) Remaining translation $t_1.\overrightarrow{X_1} + t_2.\overrightarrow{X_2}$ between the reference subset and the rotated target is measured by means of Fourier-transform based cross-correlation (FT-CC). This step is detailed in Section 4.2.3.

(4) The deformation parameters of the homography are initialized from the measured θ_0, t_1 and t_2 values. This step is detailed in Section 4.2.4.

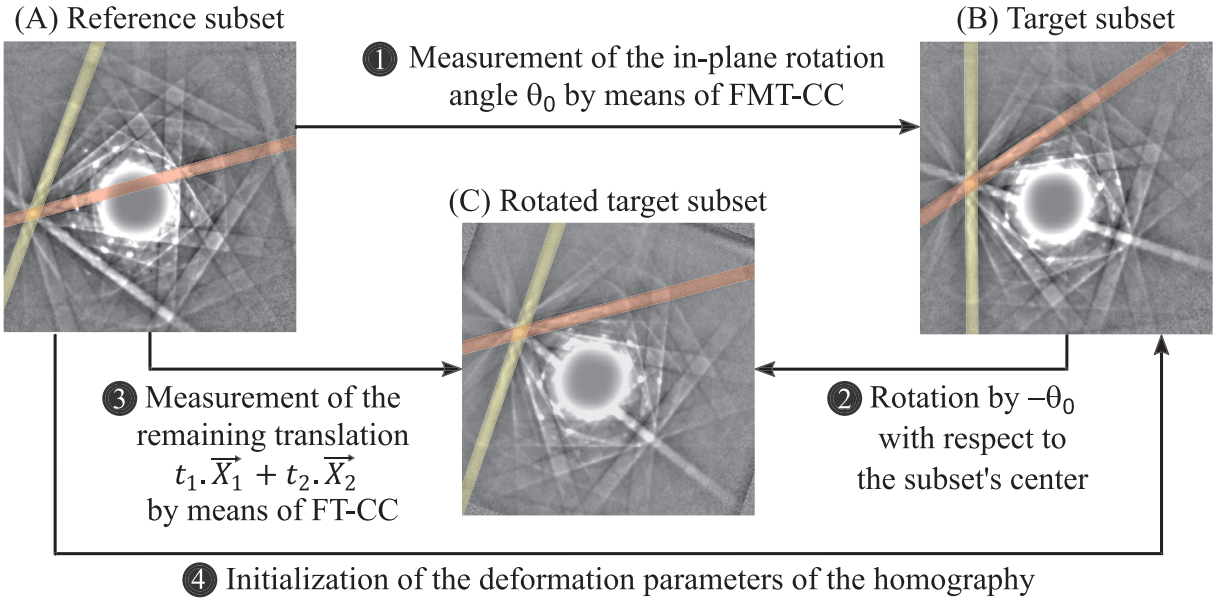

Fig. 8 Overview of the steps for pre-aligning of diffraction patterns using FMT-CC and FT-CC algorithms.

4.2 Global cross-correlation based initial guess

4.2.1 Correlation criterion and subsets' preprocessing

The zero-mean normalized cross-correlation criterion (C_{ZNCC}) is adopted:

$$C_{ZNCC}(\boldsymbol{p}) = \sum_{i=1}^{N}\left[\frac{\left[R\left(\boldsymbol{X}^{(i)}\right)-\bar{r}\right].\left[T\left(\boldsymbol{W}\left(\boldsymbol{X}^{(i)},\boldsymbol{p}\right)\right)-\bar{t}\right]}{\Delta\widetilde{r}.\Delta\widetilde{t}}\right], \tag{26}$$

where

$$\bar{r} = \frac{1}{N}\sum_{i=1}^{N} R\left(\boldsymbol{X}^{(i)}\right) \qquad \Delta\widetilde{r} = \sqrt{\sum_{i=1}^{N}\left[R\left(\boldsymbol{W}\left(\boldsymbol{X}^{(i)},\boldsymbol{p}\right)\right)-\bar{r}\right]^2}$$

$$\bar{t} = \frac{1}{N}\sum_{i=1}^{N} T\left(\boldsymbol{X}^{(i)}\right) \qquad \Delta\widetilde{t} = \sqrt{\sum_{i=1}^{N}\left[T\left(\boldsymbol{W}\left(\boldsymbol{X}^{(i)},\boldsymbol{p}\right)\right)-\bar{t}\right]^2}.$$

This is because it has the same advantages in terms of robustness to noise and affine intensity variations than the zero-mean normalized sum of square differences criterion (C_{ZNSSD}) chosen for the IC-GN algorithm (see section 4.2.3 in Chapter "Development of a homography-based global DIC approach for high-angular resolution in the SEM" by Ernould et al.). Although different, the C_{ZNCC} and C_{ZNSSD} criteria are mathematically equivalent and related as follows (Pan, Xie, & Wang, 2010):

$$C_{ZNSSD} = 2.(1 - C_{ZNCC}). \tag{27}$$

In the case of translation, the C_{ZNCC} criterion is efficiently calculated by means of the Fourier technique, as already detailed in Chapter "Measuring elastic strains and orientation gradients by scanning electron microscopy: Conventional and emerging methods" by Ernould et al. (section 3.2.2).

The user defines a square region of interest, ideally as large as possible and whose size is a power of two, so that its discrete Fourier transform is computed using an FFT (Fast Fourier Transform) algorithm. In the following, the discrete Fourier transform is referred to as the "Fourier transform" (FT) by abuse of language. Its coefficients are subject to an error, because of the finite nature of the signal. The latter does not necessarily contain a whole number of periods for each frequency. Called spectral leakage, this phenomenon is mitigated by progressively reducing to zero the intensities on the image edges. To do so, a Tukey-Hanning window (Fig. 9B)

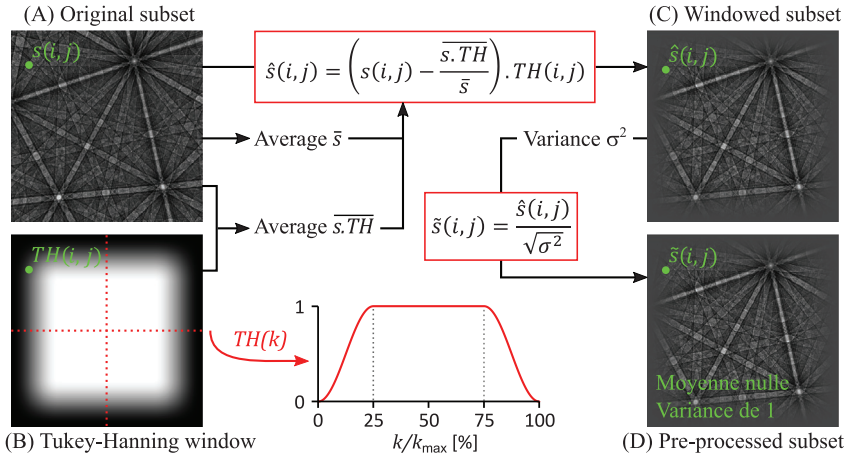

Fig. 9 Windowing and normalization of the subset's intensities before computing its discrete Fourier transform by an FFT algorithm.

$$TH(k) = \begin{cases} 1 & \text{if } 2^{n-2} + 1 \leq k \leq 3 \times 2^{n-2} \\ 0.5 - 0.5 \times \cos\left(\dfrac{4\pi.(k-1)}{2^n - 1}\right) & \text{otherwise} \end{cases} \tag{28}$$

where $n \in \mathbb{N}^*$, is applied along both directions of the original subset (Fig. 9A) of intensity s and of size $2^n \times 2^n$. The two-dimensional window is thus $TH(i,j) = TH(i)$. $TH(j)$ where $(i,j) \in [\![1, 2^n]\!]$ are the pixel coordinates. Note that any even subset size is allowed in practice, but resizing to the nearest power of two is then performed.

Because zero-mean normalized cross-correlation is considered, the subset's mean intensity and variance are equal to 0 and 1, respectively. The windowed subset of intensity $\widehat{s}$ (Fig. 9C) is consequently obtained as follows:

$$\widehat{s}(i,j) = \left(s(i,\ j) - \frac{\overline{s.TH}}{\bar{s}}\right).TH(i,j) \tag{29}$$

where $\bar{s} = \frac{1}{2^{2n}} \sum_i \sum_j s(i,j)$ and $\overline{s.TH} = \frac{1}{2^{2n}} \sum_i \sum_j [s(i,\ j).TH(i,\ j)]$.

The mean intensity of $\widehat{s}$ is zero but its intensities must still be divided by the variance

$$\sigma^2 = \frac{1}{2^{2n} - 1} \sum_i \sum_j \widehat{s}(i,j)^2, \tag{30}$$

to obtain the windowed and zero-mean normalized subset

$$\widetilde{s}(i,j) = \frac{\widehat{s}(i,j)}{\sqrt{\sigma^2}}, \tag{31}$$

i.e., the pre-processed subset (Fig. 9D) whose FT is computed.

4.2.2 Measurement of the in-plane rotation by means of FMT-CC

Now, the pre-alignment procedure is illustrated from two on-axis TKD patterns in order to discuss the influence of the central spot caused by the transmitted beam. Patterns are 600×600 pixels (Fig. 10A and A') and a 512×512 pixels subset is taken at their center and pre-treated as just detailed (Fig. 10B and B').

In-plane rotation of angle θ_0 about $-20°$ should be applied to the reference so that Kikuchi bands in red highlights are aligned. Because of such a rotation, a direct estimation of the translation by means of FT-CC fails. Indeed, the cross-correlation function (XCF) does not show any clear peak (Fig. 10F). This is because shift measurement by FT-CC is not suitable in the presence of rotation larger than $\sim 7°$ (Pan et al., 2017). Note that this justified the development of the remapping technique as part of the local

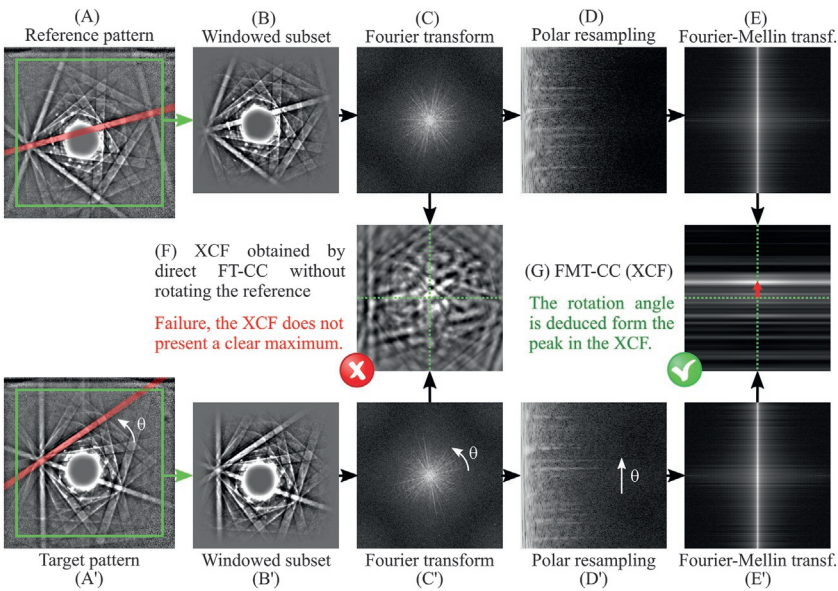

Fig. 10 Illustration of the principle of measuring in-plane rotation by means of FMT-CC by adapting the method of (Reddy & Chatterji, 1996). In this example, $\theta_0 \approx 19.6°$.

HR-EBSD/TKD approach, as discussed in Chapter "Measuring elastic strains and orientation gradients by scanning electron microscopy: Conventional and emerging methods" by Ernould et al. (section 3.2.3). On the contrary, the presence of translation is not an obstacle to the estimation of in-plane rotation by FMT-CC. Therefore, the latter algorithm is applied first.

Ways to approximate the FMT-CC are reviewed in (Derrode & Ghorbel, 2001). At this stage of development, the method by (Reddy & Chatterji, 1996) is chosen because of its simplicity. Hereafter, a slightly modified implementation is described. Scale factor being close to 1 for diffraction patterns, it is ignored to lower the computation cost of the method.

Let (x_1, x_2) be the cartesian coordinates of a point in the spatial-domain and (f_1, f_2) a point in the frequency domain. Here, coordinates (x_1, x_2) are exceptionally defined relative to the image center, not the *PC*. If an image of intensity g_r corresponds to the image of intensity g_t by the rotation of angle θ_0 around $\overrightarrow{X_3}$ and the translation $t_1.\overrightarrow{X_1} + t_2.\overrightarrow{X_2}$, then:

$$g_t(x_1, x_2) = g_r(x_1.\cos(\theta_0) + x_2.\sin(\theta_0) - t_1, -x_1.\sin(\theta_0) + x_2.\cos(\theta_0) - t_2). \tag{32}$$

In this case, their respective Fourier transforms G_r and G_t are related as follows:

$$G_t(f_1, f_2) = G_r(f_1.\cos(\theta_0) + f_2.\sin(\theta_0), -f_1.\sin(\theta_0) + f_2.\cos(\theta_0)).\ e^{-j.2\pi.(t_1.f_1 + t_2.f_2)} \tag{33}$$

according to the rotation and translation properties of the Fourier transform. Therefore, the magnitude of the Fourier transform undergoes the same rotation as the real image, as suggested by the white arrow in the lower half of Fig. 10. It is also translation invariant since this information is contained in the phase.

The Cartesian representation of the magnitude of the FT (Fig. 10C and C') is resampled in a polar frame (Fig. 10D and D'). The origin of the polar frame coincides with the center of subset center, which is also the rotation center of the FT magnitude in the Cartesian representation. This conversion makes the effects of rotation to appear as a vertical translation, as indicated by the white arrow in Fig. 10D', while a change in scale generates a horizontal translation.

Given the central symmetry of the FT magnitude in the cartesian representation, only its top two dials are resampled as schematically shown Fig. 11. The step size of the resampling is $\pi/2^n$ angularly and 0.5 pixel radially. The angular resolution thus depends on the image size. It is about 0.35° for a 512×512 pixels subset. The coordinates of the points to be sampled can be pre-calculated at the beginning of the analysis. Here, the Cartesian representation of the FT magnitude is interpolated according to a 3-point bilinear scheme which induces less artifacts than a classical bilinear interpolation while having a numerical cost almost as low (Smith, 1981).

As indicated by the green to blue color gradient, each line of the polar representation (Fig. 11B) corresponds to a given angular position (Fig. 11A). The scale factor being fixed equal to 1, only the average of the lines of the polar representation is considered. The information is thus reduced to a one-dimensional signal, which drops the numerical cost of the initial guess method. For illustration purpose, images are shown in Fig. 10E and F instead of one-dimensional signals. The lines in Fig. 10D and D' are replaced by their mean value and then the resulting image is windowed and normalized before computing its Fourier transform (Fig. 10E and E').

The cross-correlation function shows a peak whose maximum belongs to the vertical passing through the subset's center (Fig. 10G). It is located with subpixel resolution similarly to the local HR-EBSD technique. The rotation angle is finally deduced from the distance d (in pixels) between the peak maximum and the center:

$$\theta_0 = \frac{d.\pi}{2^n}. \tag{34}$$

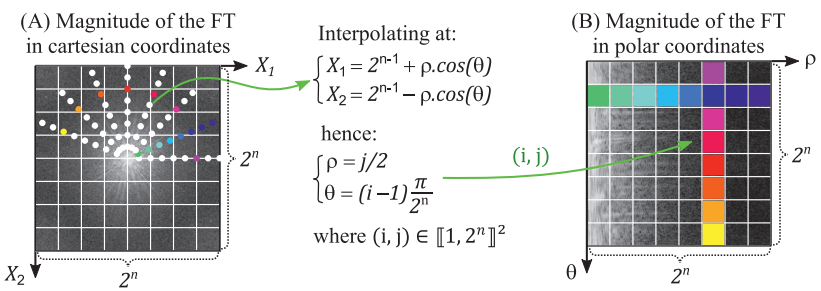

Fig. 11 Polar resampling of the two upper dials of the amplitude of the Fourier-transform (FT) in Cartesian coordinates.

4.2.3 Measurement of the remaining translation by means of FT-CC

The target subset is rotated (Fig. 12E) relative to its center X_0, by the opposite of the measured angle. As suggested by the Kikuchi bands highlighted in red and yellow, the new target subset (Fig. 12B) differs primarily by a translation from the reference subset (Fig. 12A).

Although marginal in-plane rotation is now present between the two subsets, translation measurement by FT-CC still fails (Fig. 12C). This is due to the transmitted beam which works as an anchor. It generates a parasitic and dominating peak near the XCF center, while the expect peak appears more faded in the top right dial. To remedy this, a mask containing noise is applied to the central saturated area as well as to diffraction spots contained in the reference subset (Fig. 12A'). As a result, the residual translation is correctly identified from the XCF in Fig. 12C' (green arrow). Note that the mask is still consider during the IC-GN algorithm, but points belonging to the latter are excluded from the subset.

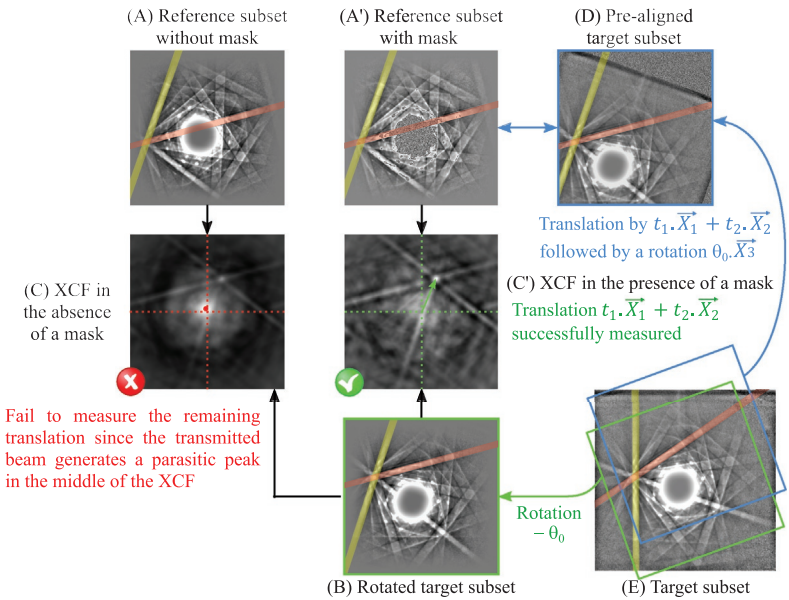

Fig. 12 Illustration of the principle of measuring the remaining translation by FT-CC. On-axis TKD patterns have a central saturated spot caused by the transmitted beam. The latter is hidden by adding a mask containing noise in the reference subset to avoid the presence of a parasitic peak in the XCF. In this example, $t_1 \approx 47$ and $t_2 \approx -111$ pixels.

4.2.4 Initialization of the homography

The approximate transformation from the reference configuration to the deformed one is obtained by the translation of parameters (t_1, t_2), followed by the rotation of angle θ_0, as shown by step 4 in Fig. 8 and in Fig. 12D. Describing the translation and rotation by the matrices $\boldsymbol{T}$ and $\boldsymbol{R}$, respectively, the initial estimate $\boldsymbol{p_0}$ of the homography is obtained by computing the transformation $\boldsymbol{R}.\boldsymbol{T}$:

$$\boldsymbol{W}(\boldsymbol{p_0}) = \boldsymbol{R}.\boldsymbol{T} = \begin{bmatrix} \cos(\theta_0) & -\sin(\theta_0) & 0 \\ \sin(\theta_0) & \cos(\theta_0) & 0 \\ 0 & 0 & 1 \end{bmatrix} . \begin{bmatrix} 1 & 0 & t_1 \\ 0 & 1 & t_2 \\ 0 & 0 & 1 \end{bmatrix}, \tag{35}$$

where

$$\begin{bmatrix} h_{11}+1 & h_{12} & h_{13} \\ h_{21} & h_{22}+1 & h_{23} \\ h_{31} & h_{32} & 1 \end{bmatrix} = \begin{bmatrix} \cos(\theta_0) & -\sin(\theta_0) & t_1.\cos(\theta_0) - t_2.\sin(\theta_0) \\ \sin(\theta_0) & \cos(\theta_0) & t_1.\sin(\theta_0) + t_2.\cos(\theta_0) \\ 0 & 0 & 1 \end{bmatrix}. \tag{36}$$

This is a "partial" initialization of the homography in that the parameters h_{31} and h_{32} are systematically zero. Only the first six parameters of the homography are initialized from the global cross-correlation measurements (t_1, t_2, θ_0). The target subset (Fig. 13D or B') is pre-aligned following a rigid transformation, i.e., a square remains a square of the same size as highlighted by the blue contours in Fig. 13E and A. With this initialization the initial residuals can nevertheless be large in the presence of high rotations due to gnomonic distortions, as shown in Fig. 13C'.

A "complete" initialization of the homography is possible by considering the projection geometry. The three rotations of the crystal w_{ij}^{IG} (IG: initial guess) in the detector reference frame are estimated from the measured rotation and translation:

$$\begin{cases} w_{32}^{IG} = \text{atan}(-\widehat{t_2}/DD) \\ w_{13}^{IG} = \text{atan}(\widehat{t_1}/DD) \\ w_{21}^{IG} = \theta_0 \end{cases} \tag{37}$$

where

$$\begin{cases} \widehat{t_1} = t_1 + x_{01}.(\cos(\theta_0) - 1) + x_{02}.\sin(\theta_0) \\ \widehat{t_2} = t_2 - x_{01}.\sin(\theta_0) + x_{02}.(\cos(\theta_0) - 1) \end{cases}. \tag{38}$$

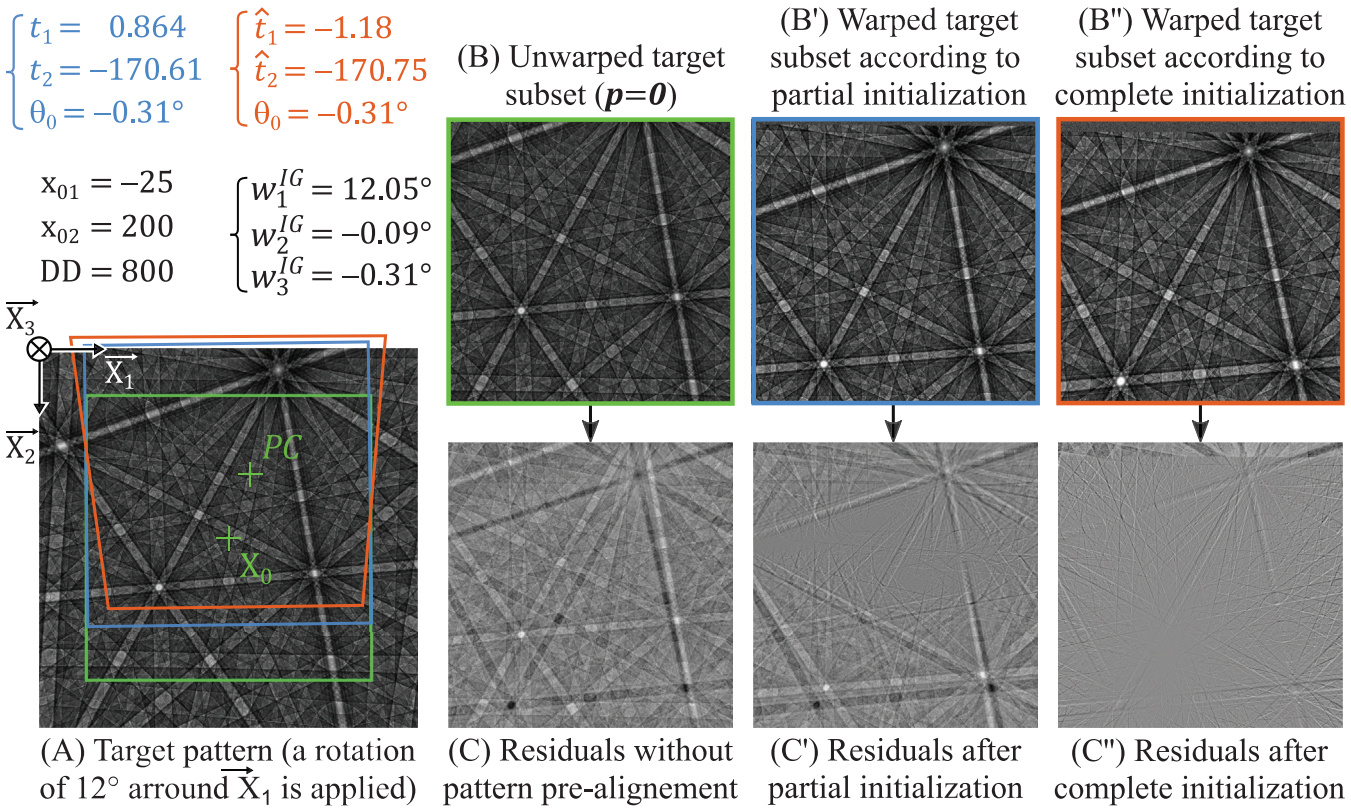

Fig. 13 (A) Target pattern undergoing 12° rotation around $\overrightarrow{X_1}$ axis relative to the reference pattern. (B) Undeformed target subset and target subset warped according to the (B′) partial initialization and (B″) complete initialization of the homography. (C-C″) Initial residuals associated with the different cases (B-B″).

The opposite of $\widehat{t_2}$ is considered in Eq. (37) because a positive rotation w_{32}^{IG} causes a global translation of the pattern along $-\overrightarrow{X_2}$. A rotation matrix $\boldsymbol{R}$ is deduced from the rotations w_{ij}^{IG} and then the deformation parameters h_{ij} are initialized from Eq. (25). As indicated by the orange outline in Fig. 13A, the full homography initialization better accounts for distortion caused by the gnomonic projection. The warped target subset (Fig. 13B'') yields to smaller residuals (Fig. 13C'') than those obtained considering the partial initialization (Fig. 13C'). This is particularly visible in the bottom of the subset, namely where the distance relative to the PC is the greatest. Overall, applying 12° rotation around $\overrightarrow{X_1}$ is a rather extreme example, which suggests the proposed global cross-correlation based initial guess is sufficiently robust for the intended applications. Its performances will be evaluated in more detail in Chapter "Numerical validation and influence of optical distortions on accuracy" by Ernould et al.

As shown in Fig. 14, the same deformed configuration materialized by a black square can be obtained from two different translations, depending on whether the prior in-plane rotation of angle θ_0 is applied with respect to X_0 (drawn in red) or the PC (drawn in blue). Crystal rotation w_{21}^{IG} $(\overrightarrow{X_3})$ in the scintillator frame rotates the pattern with respect to the PC, whereas X_0 is considered during the global cross-correlation based analysis. Therefore, this should be accounted for when estimating the two others crystal rotations w_{32}^{IG} $(\overrightarrow{X_1})$ and w_{13}^{IG} $(\overrightarrow{X_2})$. The corrected translation parameters $(\widehat{t_1}, \widehat{t_2})$ are consequently considered in Eq. (37), instead of the measured

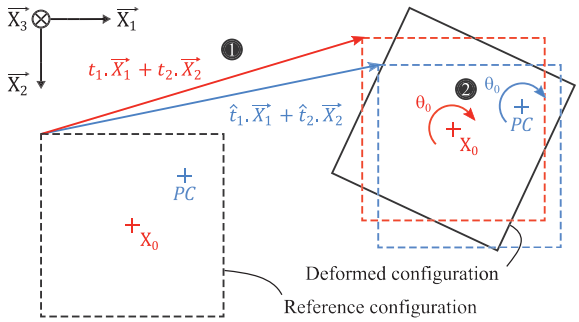

Fig. 14 Influence of the position of the center of rotation on the translation parameters describing the solid transformation. The translation (t_1, t_2) is measured considering the rotation of angle θ_0 is centered on X_0, but $(\widehat{t_1},\widehat{t_2})$ has to be considered when determining the crystal rotations, since rotation w_{21}^{IG} in the scintillator frame (i.e., with respect to $\overrightarrow{X_3}$) is centered on the PC.

ones (t_1, t_2). The correction in Eq. (38) is determined by stating that the image of a point $\boldsymbol{x} = [x_1 x_2]^T$ by a translation of parameters $(\widehat{t_1}, \widehat{t_2})$ followed by a rotation of angle θ_0 with respect to the *PC* (blue in Fig. 14), i.e.,

$$\begin{cases} \xi_1' = cos\,(\theta_0).x_1 - sin\,(\theta_0).x_2 + cos\,(\theta_0).\widehat{t_1} - sin\,(\theta_0).\widehat{t_2} - x_{01} \\ \xi_2' = sin\,(\theta_0).x_1 + cos\,(\theta_0).x_2 + sin\,(\theta_0).\widehat{t_1} + cos\,(\theta_0).\widehat{t_2} - x_{02} \end{cases} \tag{39}$$

since $\xi_i' = x_i' - x_{0i}$ ($i = 1, 2$), must coincide with the one by the rigid transformation considered by DIC measurements (red in Fig. 14):

$$\begin{cases} \xi_1' = cos\,(\theta_0).\xi_1 - sin\,(\theta_0).\xi_2 + cos\,(\theta_0).t_1 - sin\,(\theta_0).t_2 \\ \xi_2' = sin\,(\theta_0).\xi_1 + cos\,(\theta_0).\xi_2 + sin\,(\theta_0).t_1 + cos\,(\theta_0).t_2 \end{cases}. \tag{40}$$

5. Implementation in ATEX-software

The proposed HR-EBSD/TKD approach is programmed in Fortran 90. This program is contained in an executable file that is implemented in ATEX-software (Beausir & Fundenberger, 2017), developed at the authors' lab. Programming in Fortran 90 was motivated by the speed and precision of a high-level language (not interpreted). Note that applications that will be presented in Chapter "Applications of the method" by Ernould et al. are associated to datasets of 20–50 Go. The implementation could have been faster by using software like MATLAB offering many ready-to-use toolboxes (for image registration and signal processing notably). However, the extra effort result in a HR-EBSD/TKD module that does not require third-party (commercial) software to operate. Moreover, this avoids "black boxes" in the code.

ATEX-software ensures the analysis of orientation mappings. It detects grains and selects the reference points that the HR-EBSD/TKD module needs as input. As an output of the analysis, it plots the results and calculates, among other things, the intra-granular disorientation angle and the geometrically necessary dislocation densities. More generally, it proposes a graphical user interface which helps the user to define the analysis' settings. Screenshots of this interface in its current state of development are proposed in Fig. 15 (definition of the SEM configuration) and Fig. 16 (definition of the subset and others DIC settings).

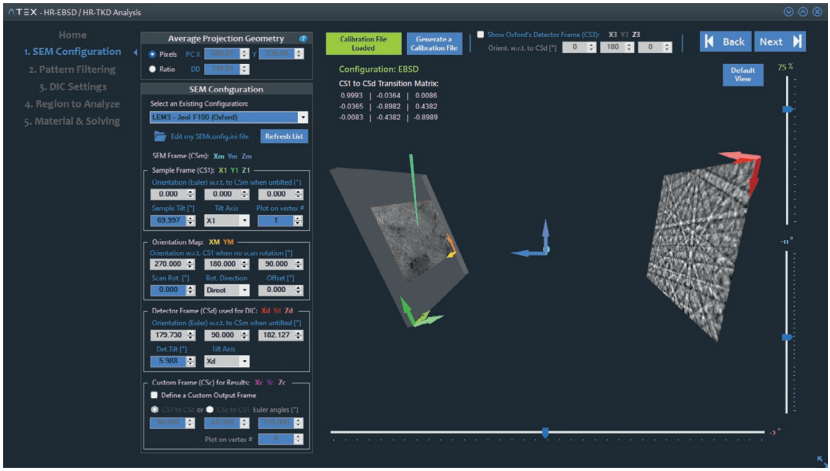

Fig. 15 Screenshot of the HR-EBSD/TKD module in ATEX-software (Beausir & Fundenberger, 2017). Definition of the SEM geometry.

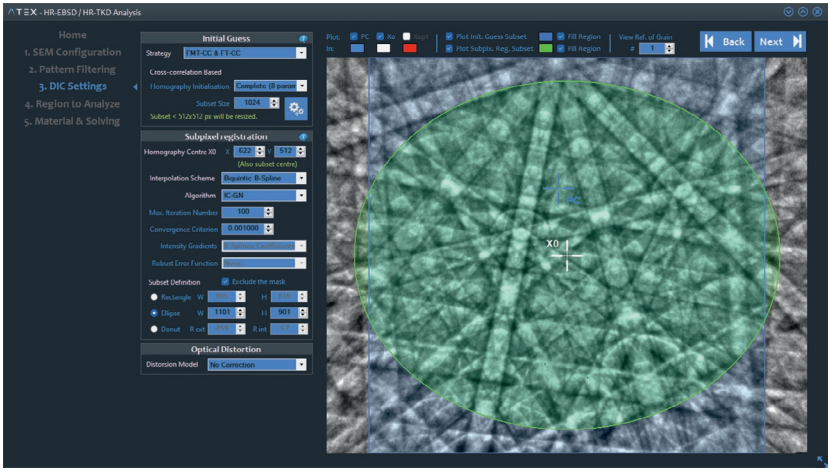

Fig. 16 Screenshot of the HR-EBSD/TKD module in ATEX-software (Beausir & Fundenberger, 2017). Selection of the DIC settings, like the shape and size of the subset used for the cross-correlation based initial guess (blue) and for the IC-GN algorithm (green).

6. Discussion

This chapter has detailed the implementation of the method through the steps of the IC-GN algorithm, the integration of a correction of optical distortions as well as the initialization of the homography, from indexing or

by means of global cross-correlation techniques. If the numerical validation of the method and its experimental application are the subject of the following chapters, some remarks can already be made concerning the possibilities of improvement of the code and the questions surrounding the choice of some parameters.

6.1 Remarks concerning the IC-GN algorithm

At this stage of development, many optimizations remain possible, starting with the parallelization of the IC-GN algorithm (Zhang et al., 2015) on graphics processing units (GPUs). Here the parallelization is performed on central processing unit (CPU) by launching several instances of the FORTRAN executable. The area to be analyzed is divided into as small tasks. They are distributed among the available cores of the CPU. As soon as one of them has finished its analysis, a new task is assigned to it.

The numerical efficiency of the IC-GN algorithm is directly related to the definition of convergence. The latter should be studied in depth.

First, the value of 0.001 pixel that recurs in the literature (Pan, 2014; Pan et al., 2013; Shao et al., 2015; Zhang et al., 2015) for the convergence criterion C_{conv} is set for affine deformations between subset a few tens of pixels wide. Therefore, the relevance of this value will be verified in the numerical validation of the method in Chapter "Numerical validation and influence of optical distortions on accuracy" by Ernould et al.

Second, no explicit expression for the norm of the increment $\boldsymbol{\Delta p}$ in the case of a linear homography has been found in the literature. Therefore, another definition than the one in Eq. (20) can be envisaged. For example, (Pan, 2014) defined the convergence in case of an affine shape function by imposing different threshold values on each of the parameters stored in $\boldsymbol{\Delta p}$. They noted this approach is stricter than a norm-based criterion. The current convergence criterion could be complemented by considering the evolution of the deformation parameters h_{ij} or their increments Δh_{ij}, after each iteration, to detect possible asymptotic behavior.

Third, one should ideally be able to evaluate the optimal value of the convergence criterion according to the data to be analyzed. Experimentally, a convergence of the IC-GN algorithm is observed in 5 to 8 iterations for $C_{conv} = 1 \times 10^{-4}$ when analyzing a GaN single crystal characterized by EBSD. This convergence criterion is rarely met in a 15% deformed IF steel, whose Kikuchi patterns are noisier and for which the diffraction contrast is blurred due to plastic deformation. This observation echoes the results of

(Vermeij & Hoefnagels, 2018). At constant convergence criterion, adding 20% noise in dynamically simulated patterns increased the number of iterations from about 5 to 120. Moreover, the mean error on elastic strains increased from $\sim 5 \times 10^{-5}$ to $\sim 8 \times 10^{-5}$. Adapting C_{conv} to data quality thus seems desirable, especially since satisfying a low convergence criterion does not necessarily provide an gain in accuracy, but unnecessarily increases the number of iterations (Pan, 2014).

Finally, implementation details can strongly affect the numerical efficiency of the IC-GN algorithm. When the first results were published (Ernould et al., 2020b), the increment $\boldsymbol{\Delta p}$ was calculated by multiplying the gradient $\boldsymbol{\nabla C_{ZNSSD}}^{IC}$ by the inverse of the Hessian matrix, as in (Pan et al., 2013). Meanwhile, solving Eq. (19) by Cholesky decomposition has significantly improved convergence speed. Optimizing performances in terms of numerical stability and efficiency requires specific know-how, going far beyond the scope and objectives of the first author's thesis.

6.2 Remarks concerning the global cross-correlation based initial estimation

Ideally, the initial estimate should be as accurate as possible since it directly affects the numerical efficiency of the IC-GN algorithm (Pan, 2018). (Ruggles et al., 2018) observed convergence in 3 to 4 iterations when the initial estimate is disoriented by 0.1°. They also noticed a rising iterations number with the initial disorientation angle. Unfortunately, this is not quantified.

The proposed patterns pre-alignment method is based on a rather rudimentary measurement principle since it does not consider gnomonic distortions. Assuming a global translation of the patterns is reasonable for small w_{23} or w_{13} rotations, but it becomes increasingly questionable as the angular disorientation increases. As shown in Fig. 13B', warping the target subset from the measured rigid transformation leads to high initial residuals ($w_{23} = 12°$). However, the measured translation is still relevant as they are significantly reduced in Fig. 13B" when considering the projection geometry. The angular accuracy of the global cross-correlation based method as well as the influence of a "partial" or "complete" initialization of the homography on convergence speed will be evaluated in Chapter "Numerical validation and influence of optical distortions on accuracy" by Ernould et al.

A compromise must be found between the accuracy of the initial estimate and its numerical cost. Otherwise, the gain in convergence speed of

the IC-GN algorithm will be cancelled out. From this point of view, the proposed pre-alignment method is based on FFT algorithms (Cooley & Tukey, 1965). Its application to 1024×1024 pixel subsets is numerically as complex as an iteration of the local HR-EBSD/TKD approach with 40 subset of size 256×256 pixels. The FFT computation of the discrete Fourier transform of an image of size $M \times M$ (where M is a power of 2) indeed has a numerical complexity of $O(M^2.\ \log_2 M)$ (Harel & Feldman, 1987) and the latter is performed 3 and 5 times during the FT-CC and FMT-CC algorithms, respectively, hence: $(3+5) \times (1024^2.\ \log_2 1024) \approx 40 \times 3 \times (256^2.\ \log_2 256)$.

The remapping technique by (Britton & Wilkinson, 2012) was not chosen because it is limited to small rotations around $\overrightarrow{X_3}$ as discussed in Chapter "Measuring elastic strains and orientation gradients by scanning electron microscopy: Conventional and emerging methods" by Ernould et al. (section 3.2.3). If (Zhu, Kaufmann, & Vecchio, 2020) proposed a more robust and accurate remapping technique, its numerical cost seems excessive in the context of an initialization of the IC-GN algorithm. According to the authors, their parallelized MATLAB code lasts between 1 and 4 s, i.e., more than the complete analysis of a point by the method proposed here (at equal pattern sizes and comparable processor frequency).

The global cross-correlation based initial guess was developed to overcome limitations of an initialization from Hough transform-based indexing. Recent advances in indexing techniques (Chen et al., 2015; Foden, Collins, Wilkinson, & Britton, 2019; Hielscher, Bartel, & Britton, 2019; Lenthe, Singh, & Graef, 2019; Nolze, Hielscher, & Winkelmann, 2017; Nolze, Jürgens, Olbricht, & Winkelmann, 2018; Winkelmann, Jablon, Tong, Trager-Cowan, & Mingard, 2020; Winkelmann, Nolze, Cios, Tokarski, & Bała, 2020) will likely allow for the avoidance of this pre-alignment procedure in the future. Actually, this step will be somehow included in indexing, since these emerging techniques are more computationally demanding than standard indexing.

To speed up dictionary indexing, (Foden et al., 2019) developed a registration method similar in spirit to the global cross-correlation approach proposed here. They refined the angular resolution of the indexing while reducing the size of the dictionary by measuring the global translation and planar rotation between the experimental pattern and the one in the dictionary that showed the highest correlation. However, the implementation of their method differs because patterns are slightly disoriented (at most by the sampling of the orientation space used to generate the library).

Translation is measured first by global FT-CC in the presence of an in-plane rotation assumed to be less than 7°. Log-polar resampling of the images (in spatial domain) is then performed, without correcting their relative translation. In-plane rotation is deduced by FT-CC from several smaller subsets, extracted from the log-polar representation rather than by considering the latter in its entirety. They reached an accuracy of typically 0.1° on the disorientation angle after two iterations for 128×128 pixels simulated patterns. Note that the four dials of the image are considered for the log-polar resampling, meaning its angular resolution of is of the order of ~2.8° (360°/128).

Their methods appear much simpler than the present one while being particularly accurate. The authors illustrated its working principle from simulated patterns, whose PC coincide with the geometric center of the image. If choosing such a particular case can be understood for the sake of illustration, the authors simply wrote: "we place the center of the log-polar transform at the screen center (placing it at the pattern center adds significant computational complexity)." Unfortunately, no general formula is given. As the same time, the authors claimed the approximation regarding the position of the center of rotation during log-polar resampling is negligible ("second order") and cited (Britton et al., 2010). They added: "it is trivial to address this issue by iterating."

On the one hand, it is no longer clear whether the fact the PC is not the image geometric center can be accounted for by using more complex formula or compensated by iterating. On the other hand, the numerical cost of the methods is affected in both cases, while domain of application is still limited to small shift and rotation. What is more disturbing is the given reference does not deal with log-polar resampling at all. Among other references, (Wolberg & Zokai, 2000) underlined the contrary: "the information derived from the polar transformation is of limited value" if the origin differs from the actual rotation center. It is precisely in order not to be affected by the presence of a possible translation and not to have any constraint on the position of the rotation center in the spatial domain, that the magnitude of the FT is considered by (Reddy & Chatterji, 1996) (see Section 4.2.2).

6.3 Remarks concerning the correction of optical distortions

The proposed correction for optical distortions echoes (Vermeij & Hoefnagels, 2018), who in 2018 emitted the possibility of optical distortions being taken into account in the Gauss-Newton algorithm.

The correction impacts the execution speed of the IC-GN algorithm by about 5–10% for a relatively complex distortion model (see Section 3.2). The difference is almost imperceptible if a simple first order radial distortion is considered. Despite this slowdown, the correction tends to reduce the overall analysis time. It is no longer necessary to pre-process all the diffraction images before the analysis, thus avoiding the calculation of the interpolation coefficients twice: once to remove optical distortion effects from the original image, and a second time to register the pre-processed image. The time saving offered by the correction depends on the number of iterations of the IC-GN algorithm and the time needed to pre-process an image, which depends mainly on the interpolation scheme. With the current code, the pre-computation of the coefficients of the biquintic B-splines of a 1200×1200-pixel Kikuchi pattern takes as long as a hundred iterations of the IC-GN algorithm with a region of interest of 901×901 pixels. Integrated correction is thus beneficial as the IC-GN algorithm typically converges in 5–15 iterations.

For the moment, only the Brown-Conrady model, i.e., Eq. (21), and its simplified versions is implemented. While it is easy to complete the list of available models, it is more difficult for an uninformed user to determine the most suitable distortion model for a given camera and to quantify its parameters. Many methods have been proposed to calibrate cameras. Among them, the one by (Dufour, Hild, & Roux, 2014) consists in reproducing a digital image on a medium and then re-matching the distorted image of this medium by the camera to its digital (undistorted) version. It employs integrated DIC techniques. The parameters of the distortion model act as deformation parameter, and a resolution up to $\sim 2.5 \times 10^{-3}$ pixels was achieved on displacements. The method is easily accommodating different distortion models. Its similarity to the global HR-EBSD technique makes it particularly interesting in that part of the code could be common to both the estimation of the distortion model and the registration of the Kikuchi patterns. Moreover, improvements of the code would then be mutually beneficial.

7. Summary

Implementation of the IC-GN according to the C_{ZNSSD}^{IC} criterion

- The IC-GN algorithm is implemented following (Blaber et al., 2015), except the considered shape function is different. It measures the

deformation parameters of the homography which minimize the zero-mean normalized sum of squared differences in the intensities, i.e., $C_{ZNSSD}{}^{IC}$ in Eq. (5). The biquintic B-splines coefficients are used for intensity interpolation and gradient computation.

- The convergence criterion C_{Conv} is set to 0.001 pixel from the literature (Pan, 2014; Pan et al., 2013; Shao et al., 2015; Zhang et al., 2015) with a maximum number of 200 iterations, although the standard is more like 30. However, further study of the convergence definition is desirable, especially to adapt it to pattern quality. The appropriateness of the value of C_{Conv} will be verified in the next chapter.

Integrated correction of optical distortions

- A correction of optical distortions is integrated in the IC-GN algorithm. It consists in a distortion model correcting the positions to be interpolated so that the deformation parameters of the homography are measured directly from optically distorted images.
- For a relatively complex distortion model, the use of the correction leads to an increase in the execution time of the IC-GN algorithm of only 5–10%, depending on the interpolation scheme used. This numerical extra cost is compensated by the absence of image pre-processing, resulting in an overall reduction in analysis time (provided that the IC-GN algorithm converges efficiently).
- The working principle of the correction is applicable to the most common distortion models. It is also transferable to other global HR-EBSD techniques based on a Gauss-Newton algorithm proposed to date (Ruggles et al., 2018; Shi et al., 2019; Vermeij & Hoefnagels, 2018).

Global cross-correlation based initial guess

- A global cross-correlation based pattern pre-alignment method was proposed to ensure efficient convergence of the IC-GN algorithm. It accounts for the effects of disorientations up to about ten degrees. For this purpose, the planar rotation θ_0 between the Kikuchi patterns is estimated by Fourier-Mellin transform-based cross-correlation (FMT-CC), and then the residual translation (t_1, t_2) is measured by Fourier transform-based cross-correlation (FT-CC).
- The deformation parameters of the homography are initialized from the measurements (θ_0, t_1, t_2). This initialization can be either "partial" $(h_{31} = h_{32} = 0)$, by considering a rigid transformation (Eq. (36)), or "complete" (Eqs. (37) and (38) combined with Eq. (25)). The latter better accounts for gnomonic distortions but requires an estimate of the projection geometry.

- This method was motivated by the occurrence of divergence of the IC-GN algorithm when initializing the homography from Hough-transform based indexing in a plastically deformed metal. The proposed approach is path independent, so it is not affected by discontinuities such as grain boundaries. Moreover, it deals with the specificities of on-axis TKD patterns (presence of diffraction spots and transmitted beam).
- Its principle being relatively simple, the numerical complexity is reasonable. It is equivalent to one iteration of the local HR-EBSD approach (using 40 subsets of 256×256 pixels). The performance of the method in the case of a partial or complete initialization of the homography will be evaluated in the next chapter.

Implementation in ATEX-software

- The proposed global HR-EBSD/TKD approach is programmed in FORTRAN to benefit from the computational speed of a non-interpreted language and not to depend on a third-party software.
- The FORTRAN program is implemented in the ATEX-software (Beausir & Fundenberger, 2017), developed in the author's laboratory. It allows the analysis of orientation maps as well as results obtained by HR-EBSD/TKD. Its graphical interface facilitates the use of the method.

References

Baker, S., & Matthews, I. (2004). Lucas-kanade 20 years on: A unifying framework. *International Journal of Computer Vision*, *56*(3), 221–255. https://doi.org/10.1023/B:VISI.0000011205.11775.fd.

Beausir, B., & Fundenberger, J.-J. (2017). *Analysis tools for electron and X-ray diffraction, ATEX—software*. Université de Lorraine. www.atex-software.eu.

Blaber, J., Adair, B., & Antoniou, A. (2015). Ncorr: Open-source 2D digital image correlation matlab software. *Experimental Mechanics*, *55*(6), 1105–1122. https://doi.org/10.1007/s11340-015-0009-1.

Britton, T. B., Maurice, C., Fortunier, R., Driver, J. H., Day, A. P., Meaden, G., et al. (2010). Factors affecting the accuracy of high resolution electron backscatter diffraction when using simulated patterns. *Ultramicroscopy*, *110*(12), 1443–1453. https://doi.org/10.1016/j.ultramic.2010.08.001.

Britton, T. B., & Wilkinson, A. J. (2012). High resolution electron backscatter diffraction measurements of elastic strain variations in the presence of larger lattice rotations. *Ultramicroscopy*, *114*, 82–95. https://doi.org/10.1016/j.ultramic.2012.01.004.

Brown, D. H. (1966). Decentering distortion of lenses. *Photometric Engineering*, *32*(3), 444–462.

Brown, D. C. (1971). Close-range camera calibration. *Photogrammetric Engineering*, *37*(8), 855–866.

Chen, Y.-H., Park, S. U., Wei, D., Newstadt, G., Jackson, M., Simmons, J. P., et al. (2015). A dictionary approach to EBSD indexing. *ArXiv*, *1502.07436* (Physics, Stat) http://arxiv.org/abs/1502.07436.

Conrady, A. E. (1919). Decentering lens systems. *Monthly Notices of the Royal Astronomical Society*, *79*, 384–390. https://doi.org/10.1093/mnras/79.5.384.

Cooley, J. W., & Tukey, J. W. (1965). An algorithm for the machine calculation of complex Fourier series. *Mathematics of Computation*, *19*(90), 297–301. JSTOR https://doi.org/10.2307/2003354.

Derrode, S., & Ghorbel, F. (2001). Robust and efficient Fourier–Mellin transform approximations for gray-level image reconstruction and complete invariant description. *Computer Vision and Image Understanding*, *83*(1), 57–78. https://doi.org/10.1006/cviu.2001.0922.

Dufour, J.-E., Hild, F., & Roux, S. (2014). Integrated digital image correlation for the evaluation and correction of optical distortions. *Optics and Lasers in Engineering*, *56*, 121–133. https://doi.org/10.1016/j.optlaseng.2013.12.015.

Ernould, C. (2020). *Développement et application d'une méthode à haute résolution angulaire pour la mesure des gradients d'orientation et des déformations élastiques par microscopie électronique à balayage [These de doctorat, Université de Lorraine]*. http://www.theses.fr/2020LORR0225.

Ernould, C., Beausir, B., Fundenberger, J.-J., Taupin, V., & Bouzy, E. (2020a). Global DIC approach guided by a cross-correlation based initial guess for HR-EBSD and on-axis HR-TKD. *Acta Materialia*, *191*, 131–148. https://doi.org/10.1016/j.actamat.2020.03.026.

Ernould, C., Beausir, B., Fundenberger, J.-J., Taupin, V., & Bouzy, E. (2020c). Characterization at high spatial and angular resolutions of deformed nanostructures by on-axis HR-TKD. *Scripta Materialia*, *185*, 30–35. https://doi.org/10.1016/j.scriptamat.2020.04.005.

Ernould, C., Beausir, B., Fundenberger, J.-J., Taupin, V., & Bouzy, E. (2021). Integrated correction of optical distortions for global HR-EBSD techniques. *Ultramicroscopy*, *221*, 113158. https://doi.org/10.1016/j.ultramic.2020.113158.

Foden, A., Collins, D. M., Wilkinson, A. J., & Britton, T. B. (2019). Indexing electron backscatter diffraction patterns with a refined template matching approach. *Ultramicroscopy*, *207*, 112845. https://doi.org/10.1016/j.ultramic.2019.112845.

Harel, D., & Feldman, Y. (1987). *Algorithmics—The spirit of computing*. Berlin Heidelberg: Springer-Verlag.

Hartley, R., & Zisserman, A. (2004). Projective geometry and transformations of 2D. *Multiple View Geometry in Computer Vision*. https://doi.org/10.1017/CBO9780511811685.005.

Hielscher, R., Bartel, F., & Britton, T. B. (2019). Gazing at crystal balls—Electron backscatter diffraction indexing and cross correlation on a sphere. *Microscopy and Microanalysis*, *25*(S2), 1954–1955. https://doi.org/10.1017/S143192761901050X.

Lenthe, W. C., Singh, S., & Graef, M. D. (2019). A spherical harmonic transform approach to the indexing of electron back-scattered diffraction patterns. *Ultramicroscopy*, *207*, 112841. https://doi.org/10.1016/j.ultramic.2019.112841.

Ma, S., Pang, J., & Ma, Q. (2012). The systematic error in digital image correlation induced by self-heating of a digital camera. *Measurement Science and Technology*, *23*(2), 025403. https://doi.org/10.1088/0957-0233/23/2/025403.

Maurice, C., Driver, J. H., & Fortunier, R. (2012). On solving the orientation gradient dependency of high angular resolution EBSD. *Ultramicroscopy*, *113*, 171–181. https://doi.org/10.1016/j.ultramic.2011.10.013.

Maurice, C., Dzieciol, K., & Fortunier, R. (2011). A method for accurate localisation of EBSD pattern centres. *Ultramicroscopy*, *111*(2), 140–148. https://doi.org/10.1016/j.ultramic.2010.10.007.

Mingard, K., Day, A., Maurice, C., & Quested, P. (2011). Towards high accuracy calibration of electron backscatter diffraction systems. *Ultramicroscopy*, *111*(5), 320–329. https://doi.org/10.1016/j.ultramic.2011.01.012.

Nolze, G., Hielscher, R., & Winkelmann, A. (2017). Electron backscatter diffraction beyond the mainstream. *Crystal Research and Technology*, *52*(1), 1600252. https://doi.org/10.1002/crat.201600252.

Nolze, G., Jürgens, M., Olbricht, J., & Winkelmann, A. (2018). Improving the precision of orientation measurements from technical materials via EBSD pattern matching. *Acta Materialia*, *159*, 408–415. https://doi.org/10.1016/j.actamat.2018.08.028.

Pan, B. (2009). Reliability-guided digital image correlation for image deformation measurement. *Applied Optics*, *48*(8), 1535–1542. https://doi.org/10.1364/AO.48.001535.

Pan, B. (2014). An evaluation of convergence criteria for digital image correlation using inverse compositional Gauss–Newton algorithm. *Strain*, *50*(1), 48–56. https://doi.org/10.1111/str.12066.

Pan, B. (2018). Digital image correlation for surface deformation measurement: Historical developments, recent advances and future goals. *Measurement Science and Technology*, *29*(8), 082001. https://doi.org/10.1088/1361-6501/aac55b.

Pan, B., Li, K., & Tong, W. (2013). Fast, robust and accurate digital image correlation calculation without redundant computations. *Experimental Mechanics*, *53*(7), 1277–1289. https://doi.org/10.1007/s11340-013-9717-6.

Pan, B., Wang, Y., & Tian, L. (2017). Automated initial guess in digital image correlation aided by Fourier–Mellin transform. *Optical Engineering*, *56*(0141031), 1–7. https://doi.org/10.1117/1.OE.56.1.014103.

Pan, B., Xie, H., & Wang, Z. (2010). Equivalence of digital image correlation criteria for pattern matching. *Applied Optics*, *49*(28), 5501–5509. https://doi.org/10.1364/AO.49.005501.

Reddy, B. S., & Chatterji, B. N. (1996). An FFT-based technique for translation, rotation, and scale-invariant image registration. *IEEE Transactions on Image Processing: A Publication of the IEEE Signal Processing Society*, *5*(8), 1266–1271. https://doi.org/10.1109/83.506761.

Ruggles, T. J., Bomarito, G. F., Qiu, R. L., & Hochhalter, J. D. (2018). New levels of high angular resolution EBSD performance via inverse compositional Gauss–Newton based digital image correlation. *Ultramicroscopy*, *195*, 85–92. https://doi.org/10.1016/j.ultramic.2018.08.020.

Shao, X., Dai, X., & He, X. (2015). Noise robustness and parallel computation of the inverse compositional Gauss–Newton algorithm in digital image correlation. *Optics and Lasers in Engineering*, *71*, 9–19. https://doi.org/10.1016/j.optlaseng.2015.03.005.

Shi, Q., Roux, S., Latourte, F., & Hild, F. (2019). Estimation of elastic strain by integrated image correlation on electron diffraction patterns. *Ultramicroscopy*, *199*, 16–33. https://doi.org/10.1016/j.ultramic.2019.02.001.

Smith, P. R. (1981). Bilinear interpolation of digital images. *Ultramicroscopy*, *6*(1), 201–204. https://doi.org/10.1016/S0304-3991(81)80199-4.

Tang, Z., Grompone von Gioi, R., Monasse, P., & Morel, J.-M. (2017). A precision analysis of camera distortion models. *IEEE Transactions on Image Processing*, *26*(6), 2694–2704. https://doi.org/10.1109/TIP.2017.2686001.

Vermeij, T., & Hoefnagels, J. P. M. (2018). A consistent full-field integrated DIC framework for HR-EBSD. *Ultramicroscopy*, *191*, 44–50. https://doi.org/10.1016/j.ultramic.2018.05.001.

Villert, S., Maurice, C., Wyon, C., & Fortunier, R. (2009). Accuracy assessment of elastic strain measurement by EBSD. *Journal of Microscopy*, *233*(2), 290–301. https://doi.org/10.1111/j.1365-2818.2009.03120.x.

Wang, J., Shi, F., Zhang, J., & Liu, Y. (2008). A new calibration model of camera lens distortion. *Pattern Recognition*, *41*(2), 607–615. https://doi.org/10.1016/j.patcog.2007.06.012.

Wilkinson, A. J., Meaden, G., & Dingley, D. J. (2006a). High resolution mapping of strains and rotations using electron backscatter diffraction. *Materials Science and Technology*, *22*(11), 1271–1278. https://doi.org/10.1179/174328406X130966.

Wilkinson, A. J., Meaden, G., & Dingley, D. J. (2006b). High-resolution elastic strain measurement from electron backscatter diffraction patterns: New levels of sensitivity. *Ultramicroscopy*, *106*(4), 307–313. https://doi.org/10.1016/j.ultramic.2005.10.001.

Winkelmann, A., Jablon, B. M., Tong, V. S., Trager-Cowan, C., & Mingard, K. P. (2020). Improving EBSD precision by orientation refinement with full pattern matching. *Journal of Microscopy*, *277*(2), 79–92. https://doi.org/10.1111/jmi.12870.

Winkelmann, A., Nolze, G., Cios, G., Tokarski, T., & Bała, P. (2020). Refined calibration model for improving the orientation precision of electron backscatter diffraction maps. *Materials*, *13*(12), 2816. https://doi.org/10.3390/ma13122816.

Wolberg, G., & Zokai, S. (2000). Robust image registration using log-polar transform. In *Proceedings 2000 International Conference on Image Processing (Cat. No.00CH37101), 1, 493–496 vol.1*. https://doi.org/10.1109/ICIP.2000.901003.

Zhang, L., Wang, T., Jiang, Z., Kemao, Q., Liu, Y., Liu, Z., et al. (2015). High accuracy digital image correlation powered by GPU-based parallel computing. *Optics and Lasers in Engineering*, *69*, 7–12. https://doi.org/10.1016/j.optlaseng.2015.01.012.

Zhu, C., Kaufmann, K., & Vecchio, K. S. (2020). Novel remapping approach for HR-EBSD based on demons registration. *Ultramicroscopy*, *208*, 112851. https://doi.org/10.1016/j.ultramic.2019.112851.